

The CNOC2 Field Galaxy Luminosity Function I: A Description of Luminosity Function Evolution

Huan Lin^{1,2,3,8}, H. K. C. Yee^{1,8}, R. G. Carlberg^{1,8}, Simon L. Morris^{4,8},
Marcin Sawicki^{1,5,8}, David R. Patton^{6,8}, Greg Wirth^{6,7,8}, & Charles W. Shepherd¹

ABSTRACT

We examine the evolution of the galaxy luminosity function (LF) using a sample of over 2000 galaxies, with $0.12 < z < 0.55$ and $17.0 < R_c < 21.5$, drawn from the Canadian Network for Observational Cosmology Field Galaxy Redshift Survey (CNOC2), at present the largest such sample at intermediate redshifts. We use $UBVR_cI_c$ photometry and the spectral energy distributions (SED's) of Coleman, Wu, & Weedman (1980) to classify our galaxies into early, intermediate, and late types, for which we compute luminosity functions in the rest-frame B , R_c , and U bandpasses. In particular, we adopt a convenient parameterization of LF evolution including luminosity and number density evolution, and take care to quantify correlations among our LF evolution parameters. We also carefully measure and account for sample selection effects as functions of galaxy magnitude and color.

Our principal result is a clear quantitative separation of luminosity and density evolution for different galaxy populations, and the finding that the character of the LF evolution is strongly dependent on galaxy type. Specifically, we find that the early- and intermediate-type LF's show primarily brightening at higher redshifts and only modest

¹Department of Astronomy, University of Toronto, 60 St. George Street, Toronto, ON M5S 3H8, Canada, lin, hyc, carlberg, sawicki, shepherd@astro.utoronto.ca

²Now at Steward Observatory, University of Arizona, 933 N. Cherry Avenue, Tucson, AZ 85721, USA, hlin@as.arizona.edu

³Hubble Fellow

⁴Dominion Astrophysical Observatory, Herzberg Institute of Astrophysics, Victoria, BC V8X 4M6, Canada, Simon.Morris@hia.nrc.ca

⁵Now at California Institute of Technology, 320-47, Pasadena, CA 91125, USA, sawicki@mop.caltech.edu

⁶Department of Physics & Astronomy, University of Victoria, P.O. Box 3055, Victoria, BC V8W 3P6, Canada, patton@uvastro.phys.uvic.ca

⁷Now at W. M. Keck Observatory, Kamuela, HI 96743, USA, wirth@keck.hawaii.edu

⁸Visiting Astronomer, Canada-France-Hawaii Telescope, which is operated by the National Research Council of Canada, the Centre Nationale de la Recherche Scientifique of France, and the University of Hawaii.

density evolution, while the late-type LF is best fit by strong number density increases at higher z , with little luminosity evolution. We also confirm the trend seen in previous smaller $z \lesssim 1$ samples of the contrast between the strongly increasing luminosity density of late-type galaxies and the relatively constant luminosity density of early-type objects. Specific comparisons against the Canada-France and Autofib redshift surveys show general agreement among our LF evolution results, although there remain some detailed discrepancies. In addition, we use our number count and color distribution data to further confirm the validity of our LF evolution models to $z \sim 0.75$, and we also show that our results are not significantly affected by potential systematic effects, such as surface brightness selection, photometric errors, or redshift incompleteness.

Subject headings: cosmology: observations — galaxies: evolution — galaxies: fundamental parameters — galaxies: luminosity function, mass function — surveys

1. Introduction

The luminosity function (LF) is a basic and fundamentally important statistic used to study galaxy populations and their evolution. In particular, measurement of the field galaxy luminosity function at different redshifts provides a simple means of describing the global changes seen in the galaxy population with lookback time. These LF data, together with complementary information from galaxy number counts and color distributions, among others, supply some of the key observations that help shape our picture of how galaxies evolve (e.g., see reviews by Koo & Kron 1992; Ellis 1997). It remains an important problem and a difficult theoretical challenge to properly interpret the variety of galaxy evolution data, including the LF, in terms of models of galaxy formation and evolution that self-consistently incorporate relevant physical processes such as star formation, feedback, and gravity (e.g., Baugh et al. 1998; Cole et al. 1994; Kauffmann et al. 1997).

Recent observational progress in measuring the field galaxy LF has spanned a very wide range of redshifts, including improved estimates using larger local ($z \sim 0$) and intermediate-redshift ($z \lesssim 1$) samples, as well as the first observations for high-redshift ($z \sim 3$) galaxies. In the local $z \lesssim 0.2$ regime, the galaxy LF is now determined routinely using redshift survey samples containing thousands of galaxies, and the LF is most commonly measured for the rest-frame optical B (Loveday et al. 1992; Marzke et al. 1994b; da Costa et al. 1994; Zucca et al. 1997; Ratcliffe et al. 1998; Colless 1998) and R bands (Lin et al. 1996a; Geller et al. 1997). However, despite the very large sample sizes, there remains controversy in the determination of the local LF, with regard to both its normalization and shape. The controversy results from potential systematic effects which may adversely affect LF measurements in local surveys at bright magnitudes; these include surface brightness selection effects, systematic photometric errors, possible local galaxy underdensities, and the small volumes over which intrinsically faint galaxies are visible (see discussion and review in Ellis 1997). The uncertainties in the local LF normalization and shape make it more difficult to

use the local results as low-redshift anchors for models of galaxy evolution. Nonetheless, a robust result from local LF measurements appears to be the dependence of the LF on galaxy type, in the sense that the faint end of the LF is consistently dominated by galaxies of later morphology (Marzke et al. 1994a; Marzke et al. 1998), later spectral type (Bromley et al. 1998; Colless 1998), stronger line emission (Lin et al. 1996a; Zucca et al. 1997), or bluer color (Marzke & da Costa 1997; Metcalfe et al. 1998).

The LF situation is somewhat less controversial at intermediate redshifts ($0.2 \lesssim z \lesssim 1$). Recent deep redshift surveys, with samples of typically hundreds of galaxies, have consistently found similar trends in the evolution of different types of galaxies (Lilly et al. 1995b; Ellis et al. 1996; Cowie et al. 1996; Lin et al. 1997; Heyl et al. 1997; Small et al. 1997; Liu et al. 1998; Hogg et al. 1998; de Lapparent et al. 1997). Namely, there exists a distinct contrast between the rapid evolution seen in the LF of late-type, blue, starforming galaxies and the relatively mild changes observed in the LF of early-type, red, quiescent objects. Also, type-dependent LF differences similar to those seen at low redshifts are also observed at intermediate z . The depth of the photometry required for intermediate-redshift surveys renders them less susceptible than their local counterparts to surface brightness selection effects, and multicolor data are also typically available for moderate-redshift samples, permitting more accurate galaxy classification. On the other hand, the sample sizes are smaller and the redshift completeness is not as high as for low- z surveys, so that the random errors on the luminosity function are in general larger than those for local LF's.

A much larger intermediate-redshift sample will, however, be provided by the Canadian Network for Observational Cosmology (CNOC) Field Galaxy Redshift Survey, hereafter denoted CNOC2. The CNOC2 survey has as its primary goal the study of the evolution of galaxy clustering and galaxy populations at intermediate redshifts $0.1 \lesssim z \lesssim 0.7$. In order to accomplish its objectives, CNOC2 will acquire some 5000 galaxy redshifts at $R_c < 21.5$, thus making a dramatic improvement over other intermediate- z surveys in terms of sample size. In addition, nearly all CNOC2 galaxies have multicolor $UBVR_cI_c$ photometry, which is more extensive color coverage than is available for the vast majority of other redshift surveys. This multicolor information permits galaxy classifications using fits to broadband colors computed from model galaxy spectral energy distributions (SED's). Consequently, luminosity functions may be calculated and studied for different galaxy populations, as well as for a number of different rest-frame bandpasses such as B , R_c , and U . In addition, the multicolor photometry permits more accurate computation of k -corrections and related quantities and also allows detailed checks of the survey's redshift completeness as functions of galaxy color and type.

In this paper we will examine the evolution of the luminosity function for different galaxy populations, using an interim but statistically complete sample of over 2000 CNOC2 galaxies with $R_c < 21.5$. Though this is only half of the ultimate CNOC2 survey sample, our interim data set nevertheless comprises the largest intermediate- z redshift survey at present. The combination of large sample size, multicolor data, and careful control of redshift selection effects should allow CNOC2 to give the best quantitative LF constraints thus far at intermediate redshifts.

The outline of the paper is as follows. In § 2 we describe details of the CNOC2 data sample, and we will also discuss redshift success rates, use of statistical weights to correct for incompleteness, and surface brightness selection effects. Then, in § 3 we detail our methods for galaxy classifications and for fitting the luminosity function and its associated evolution parameters. Our LF evolution results are described in § 4, where we focus in particular on quantifying luminosity and density evolution in the LF’s of different galaxy populations. In addition, we will also compute galaxy SED type distributions, number counts, and color distributions, as well as examine the impact that various potential systematic effects may have on our LF evolution results. In § 5, we compare our LF’s to those derived from a number of previous intermediate-redshift galaxy surveys, in particular the two next largest samples, the Canada-France Redshift Survey (Lilly et al. 1995a,b) and the composite Autofib Redshift Survey (Ellis et al. 1996; Heyl et al. 1997; plus references therein). Finally, we summarize our conclusions in § 6.

CNOC2 is now complete with respect to data acquisition, and LF studies using the full CNOC2 sample will be forthcoming once all the data have been reduced. All the *presently* available, fully reduced, and statistically complete CNOC2 data are contained in the interim sample defined below in § 2, and this is the first in a series of papers studying LF evolution in the CNOC2 data set. The second paper (Lin et al. 1999; hereafter Paper II) will address LF evolution in the context of physically-motivated galaxy evolution models. In contrast, in the present paper we focus on a *description* of the redshift-dependent changes in the luminosity function, and will not attempt to *explain* those changes in terms of physical processes; that is the province of Paper II. We emphasize that our use of “luminosity evolution” and “density evolution” should strictly be construed to describe the apparent changes in the LF, and may or may not correspond to true physical changes in individual galaxies. Not too surprisingly, it turns out that the apparent LF evolution will be sensitive to the details of the galaxy classification scheme (and choice of SED’s as a function of z) that one adopts; this will be elaborated further in § 4.1.2 and in Paper II. Nonetheless, the descriptive approach we take in this paper is a simple and effective way of characterizing and quantifying the changes in the LF’s of different intermediate-redshift galaxy populations, and it is also in essence the typical approach taken in previous LF studies.

For the Hubble constant $H_0 = 100 h \text{ km s}^{-1} \text{ Mpc}^{-1}$, $h = 1$ should be assumed in this paper if the h dependence is not explicitly shown. We also adopt a deceleration parameter $q_0 = 0.5$ throughout except where otherwise specified (in particular $q_0 = 0.1$ will be used on occasion).

2. The CNOC2 Survey Data

A detailed description of the CNOC2 Field Galaxy Redshift Survey will be given in Yee et al. (1999; see also Yee et al. 1996, 1997). We summarize the relevant points here.

The survey covers four widely separated areas, hereafter denoted as “patches”, on the sky. In this paper we use data from the two CNOC2 patches 0223+00 and 0920+37 (named by RA and

Dec). Observations for these two patches were obtained during six observing runs at the Canada-France-Hawaii Telescope (CFHT) over the period February 1995 to August 1997. Both photometry and spectroscopy were done using the CFHT Multi-Object Spectrograph (MOS). Each of these two patches is a mosaic of 19 MOS fields (each $\sim 9' \times 8'$) covering nearly 1400 arcmin^2 (but see next paragraph). Each patch is roughly in the shape of the letter L, with dimensions approximately $54'$ EW and $80'$ NS (see Yee et al. 1997).

Photometry was obtained using MOS in imaging mode for five bands (approximate 5σ limits in parentheses): Kron-Cousins R_c (24.0) and I_c (23.0), and Johnson B (24.6), V (24.0), and U (23.0). We restrict our sample to the 34 MOS fields (of the 38 total in the 0223 and 0920 patches) which have full $UBVR_cI_c$ coverage. The sky coverage of our sample is then 2490 arcmin^2 , and the comoving sample volume is $1.13(1.50) \times 10^5 h^{-3} \text{ Mpc}^3$ for $q_0 = 0.5(0.1)$. Photometric reductions (object detection, star-galaxy classification, and photometry) were done using an improved version of the Picture Processing Package (PPP; Yee 1991; Yee et al. 1996). Objects were selected in the R_c band for the survey’s spectroscopic sample and we adopt $R_c = 21.5$ as the nominal spectroscopic completeness limit (see § 2.1 below).

Multislit spectroscopy was carried out on CFHT MOS. We used a band-limiting filter to restrict the wavelength coverage to $4400\text{-}6300\text{\AA}$, in order to increase the multiplexing efficiency such that typically 90-100 objects may be observed per slit mask. The band-limiting filter does however restrict the redshift range over which spectroscopic features important for redshift measurement may be seen. We adopt the nominal redshift completeness range $0.12 < z < 0.55$, based on the observability of the Ca II H+K (3968, 3933 \AA) absorption feature important for early-type galaxies. Over this same redshift range, the [OII] $\lambda 3727$ emission feature important for late-type galaxies is also observable, except for $z \lesssim 0.2$, where we expect [OIII] $\lambda\lambda 5007, 4959$ and $H\beta$ (4861 \AA) emission to substitute for the unobservable [OII] $\lambda 3727$. Spectroscopic reductions and redshift measurements were carried out using custom-written programs and standard IRAF routines. The rms error in the velocity measurements is about 100 km s^{-1} , as determined empirically from redundant spectroscopic observations.

We correct our photometry for extinction from the Milky Way using the dust maps of Schlegel et al. (1998). We convert Schlegel et al.’s $E(B - V)$ values to magnitudes of extinction in the $UBVR_cI_c$ bands using the procedure described in their Appendix B, adopting the Milky Way extinction curves of O’Donnell (1994) and Cardelli et al. (1989). The extinction variation within each of the 0223 and 0920 patches is small, so we simply apply a single correction for each patch as a whole:

$$\left\{ \begin{array}{ccc} & 0223 & 0920 \\ \Delta U & -0.171 & -0.059 \\ \Delta B & -0.140 & -0.048 \\ \Delta V & -0.108 & -0.037 \\ \Delta R_c & -0.083 & -0.029 \\ \Delta I_c & -0.064 & -0.022 \end{array} \right. . \quad (1)$$

2.1. Redshift Success Rates and Statistical Weights

For reasons of observational efficiency, we cannot target for spectroscopy all galaxies in our fields, and like the majority of other redshift surveys, we do not successfully measure a redshift from every spectrum. We thus need to derive a set of statistical weights so that we can account for incompleteness in the CNOC2 redshift sample for our luminosity function and other analyses. Figure 1 (top left panel) shows our redshift sampling rate as a function of apparent magnitude R_c , where the redshift sampling rate is defined as the fraction of galaxies with redshifts among all galaxies in our photometric catalog. The differential redshift sampling rate is about 20% at the nominal spectroscopic completeness limit $R_c = 21.5$, and the cumulative sampling rate is about 50% for $17.0 < R_c < 21.5$. Since we do not put a spectroscopic slit on every object, the redshift sampling rate is different from the redshift success rate, defined as the fraction of *spectroscopically observed* galaxies with redshifts. Our redshift success rate is also plotted in Figure 1 (middle left panel). As expected, the redshift success rate declines with fainter apparent magnitude and hence decreasing signal-to-noise ratio in our spectra. The *raw* success rate ranges from over 90% for $R_c < 19$ to about 50% at $R_c = 21.5$, with an overall cumulative success rate of 70% for $17.0 < R_c < 21.5$. However, this raw success rate is biased low by galaxies with redshifts outside the nominal CNOC2 $0.12 < z < 0.55$ completeness range. As we will show at the end of this section, we can correct for this bias and estimate a *corrected* redshift success rate solely for $0.12 < z < 0.55$ galaxies; this improves the success rate to 70% at $R_c = 21.5$, and to about 85% cumulatively for $17.0 < R_c < 21.5$.

The simplest way to derive a statistical weight is just to use the inverse of the redshift sampling rate. This will be correct if, at each value of R_c , the spectroscopically failed objects constitute the same population as the spectroscopically successful ones, in terms of the distribution of both their spectral types and redshifts. However, this will not be true in general, as our ability to measure a redshift will be a function of the spectral type and redshift of a particular galaxy. For example, given an early- and a late-type galaxy with the same apparent magnitude R_c , the early-type galaxy will yield a lower signal-to-noise CNOC2 spectrum (4400-6300Å) because of its redder spectral energy distribution. Moreover, our finite spectral window means that our redshift failures will be biased toward objects outside of our nominal $0.12 < z < 0.55$ completeness range. We illustrate these points by plotting in Figure 1 the redshift success rate as a function of $B - R_c$ (top right panel) and $R_c - I_c$ (middle right) colors, showing that there are indeed some obvious color and hence galaxy type dependences in our success rate (but note that the same observed color can result from galaxies of somewhat different types spread out across a range of redshifts). Note in particular that the steep decline seen in the success rate for $B - R_c \gtrsim 3$ or $R_c - I_c \gtrsim 1$ is caused by higher-redshift ($z \gtrsim 0.55$) early-type galaxies whose Ca II H+K features have shifted out of our spectral window (see § 3.1). Also, the success rate drops for $B - R_c \lesssim 1$ because of lower-redshift ($z \lesssim 0.2$) late-type galaxies for which the [OII] $\lambda 3727$ emission line is likewise outside the spectral window.

One way to proceed is to apply photometric redshift methods (e.g., Sawicki, Lin, & Yee 1997; Connolly et al. 1995; Koo 1985) on our $UBVR_cI_c$ data to obtain approximate redshifts and spectral

types for all galaxies in our photometric catalog (with or without spectroscopic redshifts), and subsequently derive an estimate of our spectroscopic redshift sampling rate as a function of intrinsic galaxy type and redshift, as well as of R_c . However, this procedure will be postponed to a future paper analyzing the full 4-patch CNOC2 data set. For the present paper we adopt a simpler but sufficient procedure, and will just estimate our redshift sampling rates in joint bins of R_c , $B - R_c$, and $R_c - I_c$. Specifically, for a galaxy i which has a redshift, we will define its statistical weight W_i (the inverse of the redshift sampling rate) by

$$W_i \equiv \frac{N[R_{c,i}, (B - R_c)_i, (R_c - I_c)_i]}{N_z[R_{c,i}, (B - R_c)_i, (R_c - I_c)_i]}, \quad (2)$$

that is, just the ratio of all galaxies N to those galaxies with redshifts N_z , but where both N and N_z include only those galaxies j that lie within the following magnitude and color bounds relative to galaxy i :

$$\begin{cases} |R_{c,i} - R_{c,j}| \leq 0.25 \\ |(B - R_c)_i - (B - R_c)_j| \leq 0.25 \\ |(R_c - I_c)_i - (R_c - I_c)_j| \leq 0.1 \end{cases} . \quad (3)$$

This particular magnitude- and color-dependent weighting scheme does in fact account for our somewhat complicated redshift selection effects; that we obtain sensible results will be shown below in § 4.3 where we compare our LF-computed number counts and color distributions with the observations. Note also that we are using the sample as a whole to calculate our weights. We are thus ignoring some real field-to-field variations in our redshift success rate, due primarily to observational factors, in particular seeing. These variations need to be accounted for in galaxy clustering analyses, but should not be important for the LF analysis of this paper. A more detailed discussion of our selection effects will be found in Yee et al. (1999).

Next, we show in Figure 1 (bottom right panel) the fraction of galaxies, as a function of R_c , within our $0.12 < z < 0.55$ redshift completeness range, computed using the best-fit evolving B -band LF that we will obtain below in § 4.1. This fraction peaks at about 90% at $R_c \approx 19.5$, but declines to about 60% at $R_c \approx 17.5$ and $R_c \approx 21.5$; overall, the cumulative fraction is about 75% for $17.0 < R_c < 21.5$. We can then compute, as a function of R_c , a corrected redshift success rate $f_{\text{corrected}}$ for $0.12 < z < 0.55$ galaxies using

$$f_{\text{corrected}}(R_c) = \frac{N_z(R_c)}{N_{\text{obs}}(R_c) \times F_z(R_c)}, \quad (4)$$

where N_z is the number of galaxies with redshifts in the range $0.12 < z < 0.55$, N_{obs} is the total number of spectroscopically observed galaxies, and F_z is the LF-derived fraction of galaxies with $0.12 < z < 0.55$. This more relevant corrected success rate $f_{\text{corrected}}$ is also plotted in Figure 1 (bottom left panel), where we see that the differential rate improves to about 70% at $R_c = 21.5$ and the cumulative rate increases to about 85% for $17.0 < R_c < 21.5$. These success rates are comparable to those obtained in other large intermediate- z surveys (e.g., Crampton et al. 1995; Ellis et al. 1996). Also, in § 4.4.3 below, we discuss the impact of any potential residual z -dependent

incompleteness on our results. Finally, note that $f_{\text{corrected}}$ is computed for illustrative purposes only; it is *not* used to weight the data in any of our analyses.

2.2. Surface Brightness Selection Effects

Unaccounted surface brightness selection effects may seriously bias calculation of the luminosity function, especially for low-redshift samples with relatively shallow photometry and bright limiting isophotes (e.g., Ferguson & McGaugh 1995; Dalcanton 1998). Although surface brightness selection effects are less problematic for intermediate- z surveys like CNOC2 with deeper imaging, it is nonetheless important to quantify the survey’s effective surface brightness limits. We do so in Figure 2, where we plot apparent magnitude R_c vs. a central aperture magnitude $R_c(\text{aperture})$, for CNOC2 objects classified as galaxies or probable galaxies by PPP. $R_c(\text{aperture})$ will serve as our measure of the central surface brightness, and the aperture used is a circle with diameter $1.32''$ (corresponding to 3 pixels for our largest-pixel-size STIS2 CCD). The vertical line indicates the nominal $R_c = 21.5$ spectroscopic limit, and the horizontal line is our estimate of the central surface brightness completeness limit, $R_c(\text{aperture}) = 24.0$ (or $24.3 R_c \text{ mag arcsec}^{-2}$). The latter limit is conservatively estimated as 0.5 mag brighter than the turnover in the number count histogram for $R_c(\text{aperture})$. Also plotted is the track, as a function of redshift, for a fiducial face-on exponential disk galaxy with the Freeman (1970) central surface brightness value $\mu_{B_{AB}}(0) = 21.5 \text{ mag arcsec}^{-2}$ and an absolute magnitude $M_{B_{AB}} = -19.5 + 5 \log h \approx M_B^*$. The assumed seeing is a Moffat profile with $1''$ FWHM, nearly the CNOC2 average ($0.9''$). We calculate k -corrections using an Sbc galaxy spectral energy distribution (Coleman et al. 1980); we have checked that using an E or Im SED instead makes little difference for our conclusions.

The vast majority of our galaxies lie brightwards in central surface brightness relative to the M^* Freeman disk track, even though we should be sensitive to lower surface brightness objects; this is very similar to what Lilly et al. (1995a) found in a completely analogous plot for the Canada-France Redshift Survey. Note that our Freeman disk model is a pure exponential disk only, so that the addition of a bulge component needed for a more realistic galaxy would result immediately in a higher central surface brightness. Likewise, a sub- M^* Freeman disk or an inclined M^* Freeman disk will also have tracks that are everywhere brighter in $R_c(\text{aperture})$ (vertically below in the plot) compared to the face-on M^* Freeman disk track shown. These other tracks pass more centrally through the observed galaxy distribution, but the M^* Freeman disk track serves as a useful central surface brightness lower bound for the vast majority of galaxies.

Given the redshift track of a particular type of galaxy, our survey will be flux-limited with respect to that galaxy type *if* the track first crosses the $R_c = 21.5$ vertical boundary instead of the $R_c(\text{aperture}) = 24.0$ horizontal boundary; otherwise we will need to consider the surface brightness limit explicitly in our analyses. Figure 2 shows that we are indeed flux-limited with respect to the M^* Freeman track across the entire CNOC2 nominal redshift range $0.12 < z < 0.55$, and since that Freeman track is basically a lower surface brightness bound for the bulk of our galaxies, we

may conclude that the $R_c < 21.5$ CNOC2 photometric sample is essentially free of central surface brightness selection effects.

Also shown in Figure 2 is the track for an M^* low surface brightness (LSB) disk galaxy with $\mu_{BAB}(0) = 24.0 \text{ mag arcsec}^{-2}$, ten times fainter than that of a Freeman disk. This LSB disk crosses our central surface brightness boundary and exits our sample by $z \approx 0.25$. We are thus not complete in surface brightness to this type of LSB galaxy over the full CNOC2 redshift range. Nevertheless, as Figure 2 shows, we should still be sensitive to galaxies with somewhat higher surface brightnesses (but still fainter than the M^* Freeman track) over a fairly broad range of redshift and apparent magnitude. However, very few of these LSB galaxies faintwards of the M^* Freeman track are detected within our sample. Hence, the number of these LSB galaxies is apparently quite small compared to that of the more “normal” objects to which the survey is complete. We have not attempted to check whether the number density of our “LSB” galaxies is quantitatively consistent with recent results at low redshifts (e.g., Sprayberry et al. 1997; see review by Impey & Bothun 1997), as that would take us too far afield, requiring us to examine detailed issues of surface brightness measurements, LSB galaxy definitions, surface brightness evolution from intermediate to low redshifts, etc. We will however explore these issues in future analyses of the galaxy surface brightness distributions in the CNOC2 sample.

3. Methods

3.1. Galaxy Classification

We classify CNOC2 galaxies using least-squares fits of our $UBVR_cI_c$ colors to those computed from the galaxy spectral energy distributions (SED’s) of Coleman, Wu, & Weedman (1980; hereafter CWW). The CWW colors are computed using filter transmission curves taken from Buser & Kurucz (1978) for UBV , and from Bessel (1990) for R_cI_c . As shown in Figure 3, we assign numerical values to the four CWW SED’s as follows: 0 = E (average of the M31 bulge and M81 bulge SED’s), 1 = Sbc, 2 = Scd, 3 = Im. We linearly interpolate between neighboring SED’s using 50 equal steps in the computed broadband magnitudes, and also allow linear extrapolations to SED types -0.5 and $+3.5$. The best-fitting SED type is plotted against redshift in Figure 3 for CNOC2 galaxies with $R_c < 21.5$. The galaxies are assigned to three categories, “Early,” “Intermediate,” and “Late” according to:

$$\begin{array}{lll}
 \text{Early} & -0.50 \leq \text{SED type} < 0.50 \\
 \text{Intermediate} & 0.50 \leq \text{SED type} < 1.50 \\
 \text{Late} & 1.50 \leq \text{SED type} \leq 3.50
 \end{array} \tag{5}$$

Before fitting, we also add -0.05 mag to the I_c magnitudes computed from the E, Sbc, and Scd SED’s (but not the Im SED), in order to empirically match the observed $R_c - I_c$ colors of CNOC2 galaxies, but otherwise we make no further adjustments to the CWW SED’s. This is an ad hoc procedure and may be symptomatic of a general limitation of the CWW SED set, specifically that

they are based on a very small number of observed local galaxies which should not be expected to represent the full galaxy population in every exacting detail. However, lacking a better SED set, we nonetheless choose the CWW set for simplicity, and note that aside from the above exception, the CWW galaxy colors do give a reasonable match to the observed CNOC2 galaxy colors. In § 4.1.2, we will discuss the general implications of the particular choice of SED set and classification scheme on our galaxy evolution results. We also do not attempt to fit for dust extinction in the CNOC2 galaxies themselves (though we do correct for Milky Way extinction as described in § 2); this will be addressed instead in Paper II.

Note that our SED types are “stellar population” types derived from broadband galaxy colors, and would be more closely related to classifications derived from galaxy spectra than from galaxy morphologies. *We stress that our galaxy SED types are not and should not be interpreted as morphological types.* Of course there are correlations between galaxy types derived separately from colors, spectra, and morphologies; we postpone an examination of the similarities and differences among these various classification schemes to future CNOC2 papers.

The visual impression from Figure 3 is that there are no obvious type- or redshift-dependent incompletenesses, except for the lack of galaxies earlier than Sbc at redshifts $z \gtrsim 0.6$ (Ca II H+K redshifts out of our spectral window 4400-6300Å) and the dearth of intermediate-type galaxies at $z \lesssim 0.05$; both cases are outside our redshift completeness range $0.12 < z < 0.55$. Also, there are no redshifts at $z > 0.7$ because [OII] $\lambda 3727$ redshifts beyond the red end of our spectra. (The exceptions are a handful of higher- z AGN’s/QSO’s that are excluded from our analysis and are not plotted.) Figure 4 compares the $B - R_c$, $R_c - I_c$, $V - R_c$, and $U - R_c$ colors observed for CNOC2 galaxies with those computed from the CWW SED’s, showing that the SED’s do indeed span the range of actual galaxy colors.

We will compute absolute magnitudes, k -corrections and other needed quantities using the best-fitting (interpolated or extrapolated) CWW SED for each individual galaxy. Note in particular that the absolute magnitudes we use (in B , R_c , or U) are calculated directly from the best-fitting SED (thus making full use of the available $UBVR_cI_c$ data), rather than from any single apparent magnitude. For example, the U absolute magnitude would *not* be derived by adding $-25 - 5 \log d_L$ and a k -correction to the U apparent magnitude; instead, we would calculate the U absolute magnitude by direct integration of the best-fit SED convolved with the U -band filter response function.

3.2. Computing the LF

We compute the luminosity function using standard maximum-likelihood methods (Sandage, Tammann, & Yahil 1979; Efstathiou, Ellis, & Peterson 1988, hereafter EEP) which are unbiased by density inhomogeneities in the galaxy distribution. Our procedure essentially follows that given in Lin et al. (1996a, 1997), and is only summarized briefly here, except that we will describe in more

detail our present methods for parameterizing and fitting the *evolution* of the luminosity function.

Given a survey of N galaxies at redshifts z_i , we form the likelihood \mathcal{L} for those galaxies to possess their observed absolute magnitudes M_i :

$$\ln \mathcal{L} \equiv \ln p(M_1, \dots, M_N | z_1, \dots, z_N) = \sum_{i=1}^N W_i \ln p_i + \text{constant} . \quad (6)$$

Here W_i is the weight described previously in § 2.1, and p_i is the individual conditional probability

$$p_i \equiv p(M_i | z_i) \propto \phi(M_i) \left/ \int_{\max[M_{\min}(z), M_1]}^{\min[M_{\max}(z), M_2]} \phi(M) dM \right. , \quad (7)$$

where M_1 and M_2 are the global absolute magnitude limits we impose on the sample ($M_1 < M_i < M_2$), M_{\min} and M_{\max} are the absolute magnitude limits at z_i that correspond to the survey’s apparent magnitude limits, and $\phi(M)$ is the differential luminosity function whose parameters we determine by maximizing $\ln \mathcal{L}$.

For the form of $\phi(M)$, we adopt the usual Schechter (1976) parameterization,

$$\phi(M) = (0.4 \ln 10) \phi^* [10^{0.4(M^* - M)}]^{1+\alpha} \exp[-10^{0.4(M^* - M)}] , \quad (8)$$

with characteristic magnitude M^* , faint-end slope α , and normalization ϕ^* . We also use the nonparametric “steps” function of EEP,

$$\phi(M) = \phi_k , \quad M_k - \Delta M/2 < M < M_k + \Delta M/2 , \quad k = 1, \dots, N_p , \quad (9)$$

which we refer to hereafter as the SWML (stepwise maximum likelihood) LF. The details for computing $\phi(M)$ via maximum likelihood and for estimating errors are as given in EEP and Lin et al. (1996a, 1997).

To parameterize evolution in the luminosity function, we adopt the following simple model for the redshift dependence of the Schechter parameters:

$$\begin{aligned} M^*(z) &= M^*(0) - Qz \\ &= M^*(z = 0.3) - Q(z - 0.3) \\ \alpha(z) &= \alpha(0) \\ \rho(z) &= \rho(0)10^{0.4Pz} . \end{aligned} \quad (10)$$

We thus take M^* to vary linearly with redshift, at a rate quantified by Q , which we call the M^* or luminosity evolution parameter. Note that we will fit for $M^*(z = 0.3)$ since this is a better constrained quantity than $M^*(0)$, given the mean redshift $z \approx 0.3$ for CNOC2 galaxies. We also make the null assumption that α does not change with redshift, so that the shape of the LF stays the same. Since α is fixed, the normalization parameter ϕ^* and the total galaxy number density $\rho = \int \phi(M) dM$ are essentially equivalent. We then take ρ to vary with z as determined by the

density evolution parameter P defined above. The expression for ρ in equation (10) is chosen for convenience, so that the luminosity density $\rho_L = \int L\phi(M)dM$ (where $L \propto 10^{-0.4M}$) may be written as:

$$\rho_L(z) = \rho_L(0)10^{0.4(P+Q)z} , \quad (11)$$

where $P + Q$ then measures the linear rate of evolution of ρ_L with redshift. Also, note that ρ as defined above may be approximated by $\rho(z) \approx \rho(0)(1 + Pz)$, so that P is merely the coefficient of the linear term in the expansion of ρ in powers of z .

We first estimate $M^*(z = 0.3)$, α , and Q together using the usual maximum likelihood method, and by design this is independent of density fluctuations or density evolution, so that both $\phi^*(0)$ and P have to be determined separately, beginning with P . In the case of a non-evolving LF, it is possible to derive maximum-likelihood estimates of $\rho(z)$ without prior knowledge of the luminosity function (Saunders et al. 1990; Loveday et al. 1992; Fisher et al. 1992). This is completely analogous to the case above where we may estimate M^* and α independently of galaxy density variations. For the more general evolving LF defined above, we may still determine P without knowing $M^*(z = 0.3)$ or α , but not without first knowing Q . Given a value of Q , we may convert an observed absolute magnitude M_i at $z = z_i$ to an evolution-corrected absolute magnitude at some fiducial redshift, say $z = 0$ (the actual redshift does not matter): $M_i(0) \equiv M_i(z_i) + Qz_i$. Then, with any given Q and the resulting set of $M_i(0)$, we compute the likelihood that those galaxies will have their observed redshifts z_i :

$$\ln \mathcal{L}' \equiv \ln p'(z_1, \dots, z_N | M_1(0), \dots, M_N(0), Q) = \sum_{i=1}^N W_i \ln p'_i + \text{constant} . \quad (12)$$

Here the individual conditional probabilities are (cf. Saunders et al. 1990; Fisher et al. 1992)

$$\begin{aligned} p'_i &\equiv p(z_i | M_i(0), Q) \\ &\propto \phi'(M_i(0), z = 0) \rho(z_i) \left/ \int_{\max[z_{\min}(M_i(0)), z_1]}^{\min[z_{\max}(M_i(0)), z_2]} \phi'(M_i(0), z = 0) \rho(z) \frac{dV}{dz} dz \right. \\ &= \rho(z_i) \left/ \int_{\max[z_{\min}(M_i(0)), z_1]}^{\min[z_{\max}(M_i(0)), z_2]} \rho(z) \frac{dV}{dz} dz \right. \\ &= 10^{0.4Pz_i} \left/ \int_{\max[z_{\min}(M_i(0)), z_1]}^{\min[z_{\max}(M_i(0)), z_2]} 10^{0.4Pz} \frac{dV}{dz} dz \right. , \end{aligned} \quad (13)$$

where ϕ' is ϕ with ϕ^* set to unity (ϕ' has units of mag^{-1}), z_1 and z_2 are the global redshift limits we impose on the sample, and z_{\min} and z_{\max} are the redshift limits over which galaxy i may be observed, given the survey's apparent magnitude limits and the assumed rate of evolution specified by Q . P may then be readily determined using maximum likelihood, once given the previously found best-fit value for Q . The fifth and final parameter $\phi^*(0)$ is then computed via straightforward summation (cf. Lin et al. 1996a, 1997)

$$\phi^*(0) = \frac{1}{V} \sum_i \frac{W_i}{S(z_i)10^{0.4Pz_i}} \left/ \int_{M_1}^{M_2} \phi'(M, z = 0) dM \right. , \quad (14)$$

where V is the survey volume and $S(z)$ is the selection function, defined by

$$S(z) \equiv \int_{\max[M_{\min}(z), M_1]}^{\min[M_{\max}(z), M_2]} \phi(M, z) dM \bigg/ \int_{M_1}^{M_2} \phi(M, z) dM . \quad (15)$$

Once we have fit for all the LF parameters, we will calculate luminosity densities ρ_L as a function of redshift using

$$\rho_L(z_a < z < z_b) = \frac{1}{V(z_a < z < z_b)} \sum_{z_a < z_i < z_b} W_i 10^{-0.4M_i} / S_L(z_i) , \quad (16)$$

where

$$S_L(z) = \int_{\max[M_{\min}(z), M_1]}^{\min[M_{\max}(z), M_2]} 10^{-0.4M} \phi(M, z) dM \bigg/ \int 10^{-0.4M} \phi(M, z) dM . \quad (17)$$

That is, we sum over the luminosities of our observed galaxies, but weighted by the factor $S_L(z)$, which uses the luminosity function ϕ to extrapolate for the luminosity of unobserved galaxies lying outside the accessible survey flux limits. Also, we will express ρ_L in units of $h \text{ W Hz}^{-1} \text{ Mpc}^{-3}$ using the conversion given in Lilly et al. (1996); specifically, one $M_{BAB} = -19.5 + 5 \log h$ galaxy per Mpc^3 produces a luminosity density of $2.85 \times 10^{21} h^{-2} \text{ W Hz}^{-1} \text{ Mpc}^{-3}$.

Finally, we estimate uncertainties in ρ_L and $\phi^*(0)$ using both bootstrap resampling and an estimate of the uncertainty contributed by galaxy density fluctuations. We apply bootstrap resampling (e.g., Barrow et al. 1984) to the *full photometric* sample (not just to those galaxies with redshifts), re-calculate statistical weights W_i (as in § 2.1) anew for galaxies with redshifts in each bootstrap resample, and then re-fit our LF evolution model and re-compute luminosity densities. This process should account for the uncertainties in $\phi^*(0)$ and $\rho_L(z)$ contributed by sampling and weighting fluctuations and by our fitting procedure. This does not account for the additional uncertainty arising from galaxy density fluctuations, which we estimate instead using an integral over the galaxy clustering power spectrum $P(k)$; see § 3 of Lin et al. (1997) for details. For $P(k)$ we adopt the local result from the Las Campanas Redshift Survey (Lin et al. 1996b, eqs. [23,24]), but adjusted (only) for the *linear* clustering evolution at the higher redshifts sampled in CNOC2; this is done as appropriate for both the $q_0 = 0.5$ and 0.1 cosmologies we consider. We then take the overall error on $\phi^*(0)$ and ρ_L to be the quadrature sum of the bootstrap resampling and density fluctuation error contributions.

4. Results

4.1. Evolution of the B_{AB} -band LF

We apply the LF fitting methods and evolution model of § 3.2 to our nominally complete $17.0 < R_c < 21.5$ sample, subdivided into early, intermediate, and late galaxy types as described in § 3.1. The sample details and fit parameters are given in Table 1. We first concentrate on our LF

results in the B band, shown in Figure 5 for the three galaxy types and for each of three redshift bins in the range $0.12 < z < 0.55$. For ease of comparison against previous surveys, we will report our B -band LF results in the AB system (Oke 1972) using the transformation $B_{AB} = B - 0.14$ (Fukugita et al. 1995). The points in the figure show the nonparametric SWML LF estimates in each individual type-redshift bin, while the solid lines indicate the results of our 5-parameter LF evolution model ($M^*(z = 0.3)$, α , $\phi^*(0)$, P , and Q), fit to the full redshift completeness range $0.12 < z < 0.55$ for each of the three galaxy types. Figure 5 should allow us to judge how well our parametric LF model matches the nonparametric LF estimates, which we obtained without making any assumptions about the form that the LF evolution takes.

4.1.1. Some Technical Considerations

There are, however, a number of subtleties involved in comparing the SWML LF estimates ϕ_k to the parametric evolving LF estimate $\phi(M, z)$. The nonparametric ϕ_k are binned in both M and z , while the parametric $\phi(M, z)$ is not, and it may be unclear at what redshift we should evaluate $\phi(M, z)$ in order to compare against the ϕ_k . For example, a simple procedure such as plotting the parametric LF models evaluated at the average redshift of each redshift bin in Figure 5 will actually result in noticeable discrepancies (at the bright and faint ends of the LF) when compared against the ϕ_k , even when there should be none. The proper thing to do is actually to calculate a weighted average of $\phi(M, z)$ over the appropriate intervals in M and z . Specifically, we follow a procedure given by EEP, but modified for our sample. We note first that in general $\phi_k \neq \phi(M = M_k)$, even in the absence of LF evolution. As shown by EEP in their equation (2.15), the ϕ_k are actually related to the parametric $\phi(M)$ by a weighted integral over $\phi(M)$, where the weights are just the expected number $N(M)$ of galaxies of absolute magnitude M observable by the survey. In the limit that the bin size $\Delta M \rightarrow 0$, and with no evolution, ϕ_k would indeed converge to $\phi(M = M_k)$. For CNOC2 we need to modify EEP’s original equation (2.15) to account for our use of an evolving LF, as well as for cosmological and k -correction effects important for our intermediate- z sample. Specifically, for an absolute magnitude bin $M_k - \Delta M/2 < M < M_k + \Delta M/2$ and a redshift bin $z_1 < z < z_2$, we may define the quantity

$$\begin{aligned} \phi_{\text{parametric},k}(z_1 < z < z_2) &\equiv \int_{M_k - \Delta M/2}^{M_k + \Delta M/2} \int_{\max[z_{\min}(M), z_1]}^{\min[z_{\max}(M), z_2]} \phi(M, z) \frac{dN}{dz dM}(M, z) dz dM \\ &\int \int_{M_k - \Delta M/2}^{M_k + \Delta M/2} \int_{\max[z_{\min}(M), z_1]}^{\min[z_{\max}(M), z_2]} \frac{dN}{dz dM}(M, z) dz dM \quad (18) \end{aligned}$$

$$\begin{aligned} &= \int_{M_k - \Delta M/2}^{M_k + \Delta M/2} \int_{\max[z_{\min}(M), z_1]}^{\min[z_{\max}(M), z_2]} \phi^2(M, z) \frac{dV}{dz} dz dM \\ &\int \int_{M_k - \Delta M/2}^{M_k + \Delta M/2} \int_{\max[z_{\min}(M), z_1]}^{\min[z_{\max}(M), z_2]} \phi(M, z) \frac{dV}{dz} dz dM \quad , \quad (19) \end{aligned}$$

where $\frac{dN}{dM}(M, z) = \phi(M, z)dV$ is the expected number of galaxies per unit magnitude at redshift z , and $z_{\min}(M)$ and $z_{\max}(M)$ are the minimum and maximum redshift, respectively, at which a galaxy of absolute magnitude M may be seen, given our survey’s apparent magnitude limits and cosmological and k -correction effects. The parametric LF estimates we plot in Figure 5 and elsewhere are those given by Equation (19); this is the right way to compare our parametric LF fits against the directly-computed nonparametric SWML estimates.

In addition, in Figure 5 we also show low-redshift fiducial LF’s (dotted curves) to facilitate comparison from one redshift bin to another. For this purpose we use $\phi(M, z = 0.175)$ (i.e., ϕ evaluated at nearly the average redshift of the lowest- z bin), but appropriately averaged using Equation (19) over the higher-redshift intervals. Also to facilitate bin-to-bin comparisons, we show extrapolations (dashed curves) of the parametric LF’s faintwards of the faintest absolute magnitude accessible in each redshift bin. For this purpose we simply choose $\phi(M, z = (z_1 + z_2)/2)$ (i.e., ϕ evaluated at the average redshift of the bin), since $\phi_{\text{parametric},k}$ defined above is zero at these magnitudes (no galaxies observable there!). Note the slight disconnections between the solid and dashed curves for the late-type parametric LF’s in the two highest- z bins in Figure 5; these are artificial and are examples of the “noticeable discrepancies” mentioned above.

For clarity in seeing the evolution trends, we have purposefully matched the normalizations of the SWML and parametric LF fits in each redshift bin of Figure 5. Specifically, we set

$$\sum_{k=1}^{N_p} \phi_k V(M_k) = \sum_{k=1}^{N_p} \phi_{\text{parametric},k} V(M_k) , \quad (20)$$

where $V(M_k)$ is the volume (within the redshift limits of each bin) over which a galaxy of absolute magnitude M_k may be seen in our survey. We do this to take out the effects of strong density fluctuations present in the survey, clearly seen in the (weighted) redshift histograms shown in Figure 6 (left panels), particularly for early- and intermediate-type galaxies in the $0.25 < z < 0.4$ bin. Note from Figure 6 (right panels) that the ratio of actual to LF-computed redshift distributions are reasonably centered on unity and do not show conspicuous systematic trends with redshift, indicating that the normalization $\phi^*(0)$ and the number density evolution parameter P in our fits are indeed good matches to the data. (To construct the galaxy redshift histograms, we have first weighted each galaxy by W_i to correct for redshift incompleteness; this makes construction of the corresponding LF-computed redshift histogram much simpler, since we are then freed from modeling the somewhat complicated magnitude- and color-dependent selection effects of our survey.)

4.1.2. Description of the LF Evolution

Setting the above technical considerations aside and returning to Figure 5, we may note that our LF model does indeed appear to be a reasonable description of the data, as seen in the good agreement between the parametric and nonparametric SWML fits (but recall we have matched their normalizations, so that we are really only assessing the validity of the M^* , α and Q parameters).

The comparison also shows that our simple assumption of a fixed α is quite reasonable, though of course at higher redshifts it becomes increasingly difficult to constrain the faint-end slope of the luminosity function. Note also that our fixed- α result differs from that found in the Autofib Redshift Survey (Ellis et al. 1996; Heyl et al. 1997); see § 5.3 below.

Figure 5 also shows that the three galaxy types have conspicuously different LF’s, with faint-end slopes α steepening from $\alpha = +0.1$ for early types to $\alpha = -1.2$ for late types (Table 1). These clear LF differences are indeed significant, as shown in Figure 7 (top panel), where we see non-overlapping or barely-touching 2σ error contours in $M^*(z = 0.3)$ and α for the three galaxy types.

Figure 5 demonstrates that the LF’s for all three galaxy types do indeed evolve. The impression is that the early- and intermediate-type LF’s are not changing much in number density, but are rather brightening in M^* at higher redshifts. For the late-type LF, it is harder to discern visually (because of the steepness of the LF) whether the definite changes seen result from increasing number density, brightening M^* , or a combination of the two. We can isolate the luminosity evolution component of the LF’s by rescaling the dotted fiducial $z = 0.175$ LF in each panel by the factor $10^{\{0.4P[(z_1+z_2)/2-0.175]\}}$, to explicitly take out the effect of the number density evolution parameter P . We do this in Figure 8, where we confirm our earlier impression that the early- and intermediate-type LF’s are evolving primarily in M^* . In contrast, the rescaled low- z fiducial late-type LF is a good match to the results in the two higher-redshift bins, indicating that the observed late-type LF evolution seen before in Figure 5 is driven primarily by number density changes. (Note that an apparent change in number density does not necessarily imply mergers; changes in the star formation duty cycle for late-type galaxies may also mimic the effect of true mergers.)

Now, an important consideration mentioned in the Introduction needs to be kept in mind, namely the sensitivity of the LF evolution results to the precise *choice* of SED’s used to classify galaxies. In particular, the present choice of *non-evolving* CWW SED’s obviously does not account for the evolution of the colors of galaxies with time, so that during the course of its evolution, a particular galaxy may actually cross the type boundaries we have defined. It is thus better to use more physically motivated *evolving* galaxy SED’s (e.g., produced by models such as those of Bruzual & Charlot 1996) to properly track the paths different galaxies may take in the space of redshift vs. color. Not surprisingly, the resulting galaxy classifications will in general differ from the ones we make based on the CWW SED’s, and importantly, the conclusions we draw on the rates of luminosity and density evolution for different galaxy populations will also be different in general. However, there are a myriad of possible evolving SED’s that one may choose by varying parameters such as star formation history, stellar initial mass function, epoch of galaxy formation, metallicity, dust content, and others, so that there is no unique set of SED’s that one should obviously pick a priori. In LF Paper II, we will examine evolution in the CNOC2 sample using these physically motivated evolving galaxy SED models. In the present paper, though, we will use only the non-evolving CWW SED’s for galaxy classification. Thus, the LF evolution constraints we derive here should strictly be considered as *descriptions* of galaxy evolution within the framework

of non-evolving SED’s, rather than as *explanations* of galaxy evolution in terms of more physically motivated processes. In other words, we are using the terms “luminosity evolution” and “density evolution” purely to describe the changes in the LF’s of the galaxy populations we have defined, and those terms *may* not correspond to the true evolutionary processes those galaxies are actually undergoing. (The latter is not precluded, though. As we will find in Paper II, the luminosity evolution we see in early and intermediate galaxies still holds true when we use physically-motivated evolving SED’s.)

Also, we caution that the LF constraints will be weaker and the errors larger when our LF models are extrapolated outside the nominal CNOC2 redshift limits. For example, the errors are approximately doubled for $M^*(z = 0)$ compared to $M^*(z = 0.3)$; specifically $M^*(z = 0) = -18.58 \pm 0.23$, -19.11 ± 0.34 , and -19.20 ± 0.35 for early-, intermediate-, and late-type galaxies, respectively. There are only about 200 galaxies in our LF sample with $0.12 < z < 0.2$ to constrain the lowest- z behavior of our LF evolution model. These galaxies alone do in fact give an overall best fit $M_{BAB}^* = -19.5$ and $\alpha = -0.9$, in reasonable agreement with results from much larger local redshift samples (e.g., Loveday et al. 1992), and our $M^*(z = 0)$ and α values for intermediate- and late-type galaxies are also in good agreement with local results (e.g., Figure 8 of Colless 1998). However, our early-type LF may have a fainter $M^*(z = 0)$ and shallower α compared to local values (e.g., Colless 1998, but cf. also Bromley et al. 1998). In future work we will compare in more careful detail our results with those of large local surveys, in order to further check the validity of extrapolations of our LF models (see also §§ 4.3 and 5.2).

Keeping the above caveats in mind, our impression so far is that evolution in early- and intermediate-type galaxies is dominated by brightening in M^* at higher z , while the evolution in late-type galaxies is caused by increasing number densities at higher redshifts. This impression is borne out in the P vs. Q error contours shown in Figure 9: early and intermediate types show positive luminosity evolution, with a combined $Q = 1.3$, but little density evolution, $P = -0.3$, while late types show strong positive density evolution, $P = 3.1$, but little M^* evolution, with $Q = 0.2$ (Table 1). However, Figure 9 also shows that we need to be somewhat cautious, and keep the correlated nature and fairly large size of the P - Q error contours in mind. Not surprisingly, our ability to decouple density and luminosity evolution depends on the shape of the luminosity function: for early and intermediate types, the LF has a shallow α and a conspicuous “knee” near M^* , while for late types the LF is steep and it becomes correspondingly harder to measure subtle changes in M^* with redshift. Thus, although the late-type sample is the largest among the three types, the late-type P - Q contour is the most elongated and the most difficult one for which to separately constrain density and luminosity evolution. Moreover, even for the two earlier-type samples, no-evolution ($P = 0$, $Q = 0$) is ruled out at only somewhat better than the 2σ level. Nonetheless, it does appear to be a fairly robust conclusion from Figure 9 that late types occupy a different region of P - Q parameter space than early and intermediate types, so that the form of the LF evolution of late-types is distinct from that of early- and intermediate-type galaxies,

4.1.3. Evolution of the Luminosity Density

Despite the difficulties in decoupling P and Q , we can nevertheless robustly constrain the sum $P + Q$, which measures the rate of evolution of the rest-frame luminosity density $\rho_L(z)$. The error contours in Figure 9 are elongated roughly along lines of constant $P + Q$ (and thus compressed in the orthogonal direction), so that the contours are actually most effective for constraining the sum as opposed to P and Q separately. The luminosity density of late types evolves at a significantly more rapid rate ($P + Q = 3.3$) than that of early and intermediate types ($P + Q = 0.5$ and 1.6 , respectively). This is shown in more detail in Figure 10, where we plot $\rho_L(z)$ for the 3 galaxy types individually, as well as summed together. We also tabulate our luminosity density results in Table 3. Clearly, the late-type population shows the most strongly increasing $\rho_L(z)$, while the early and intermediate types show much milder increases at higher redshift. Note that the luminosity densities for the three types are roughly equal at $z \approx 0.1$, but by $z \approx 0.55$ late-type galaxies predominate and account for over half of the total luminosity density. Also shown in Figure 10 are the separate contributions to $\rho_L(z)$ from the luminosity and number density evolution components for each of the three galaxy types. Compared to the P - Q plot or even the LF plots, the curves for these individual components most clearly illustrate the different LF evolution trends we discussed earlier (but keeping the caveats in mind). The late-type galaxy LF is dominated by strong density evolution, with nearly no luminosity evolution. The intermediate-type LF shows positive luminosity evolution plus weak positive density evolution, resulting in mild positive evolution in ρ_L . The early-type LF shows positive luminosity evolution which is nearly compensated by negative density evolution, yielding a very weak positive evolution in the luminosity density.

These general conclusions are not altered much by adopting a $q_0 = 0.1$ instead of a $q_0 = 0.5$ cosmology. Our $q_0 = 0.1$ results are also tabulated in Tables 1 and 3, and the corresponding P - Q contours and $\rho_L(z)$ plots are shown in Figures 11 and 12, respectively. To first order, absolute magnitudes change with q_0 as $M(z, q_0) \approx M(z, q_0 = 0.5) + (q_0 - 0.5)z$, and the differential volume element varies as $\frac{dV}{dz}(z, q_0) \approx \frac{dV}{dz}(z, q_0 = 0.5)[1 - 2(q_0 - 0.5)z]$. We thus expect $\Delta Q \approx +0.4$, $\Delta P \approx -0.8$, and $\Delta(P + Q) \approx -0.4$ in going from $q_0 = 0.5$ to $q_0 = 0.1$, and indeed that is what we approximately find quantitatively. Qualitatively, this means more positive luminosity evolution, but more negative number density and luminosity density evolution. In particular, no-evolution ($P = Q = 0$) for the early and intermediate types combined may be ruled out at higher significance than was possible for the $q_0 = 0.5$ case. Otherwise, though, the general LF evolution trends follow those for the $q_0 = 0.5$ cosmology.

Finally in this subsection, we make the most minimal assumptions and fit the LF for the three galaxy types with non-evolving Schechter functions, and compare the resulting trends of luminosity density vs. redshift against those obtained from the evolving models above; this is done in Figure 13 (for $q_0 = 0.5$ only). Reassuringly, we find that the actual trend of ρ_L with redshift (the *points* in the figure, not the curves) is insensitive to whether we use non-evolving or evolving LF's (in eqs. [16] and [17]). The late-type ρ_L always rises sharply compared to the weak increases observed for the earlier types. However, as seen in the top two panels of Figure 13, a constant ρ_L , as required by

a non-evolving LF, is clearly a bad description of the late-type $\rho_L(z)$, and consequently for the total $\rho_L(z)$ as well, since late types make up the greatest contribution. On the other hand, a non-evolving constant $\rho_L(z)$ does seem to be reasonable for the two earlier types. This is not surprising, as Figure 9 shows that although an evolving LF is preferred by the data, a non-evolving LF is ruled out at only about 2σ for early and intermediate galaxies. A larger data set will be needed in order to make a stronger statement regarding no-evolution vs. evolution, and the doubled size of the final CNOC2 sample should allow significantly improved constraints on these early- and intermediate-type galaxies. In addition, we are also calibrating photometric redshifts using the multicolor data for our spectroscopic-redshift sample. Application of photometric redshifts to those CNOC2 galaxies without spectroscopic redshifts should provide another factor of two increase in the number of $R_c < 21.5$ galaxies that may be used in our LF studies, thereby allowing further improvements in our evolution constraints.

4.2. The R_c - and U -band LF's

The availability of $UBVR_cI_c$ colors in conjunction with the CWW SED types makes it a straightforward matter to calculate the appropriate k -corrections and derive the LF in bands other than B , the most typical choice. We do so for the R_c and U bands. No extrapolations are required of our color data to derive rest-frame U magnitudes. Although extrapolations are required to obtain rest-frame R_c magnitudes, the needed k -corrections are not large ($\lesssim 1$ mag) and are well-constrained by the SED classifications. Note that here we are always using a $17.0 < R_c < 21.5$ sample; we are *not* varying the band used for galaxy *selection* (not until §§ 4.5 and 5.3 below)

The best-fit R_c and U LF and evolution parameters are given in Table 2, and the luminosity densities are given in Table 3. The R_c - and U -band LF's themselves will not be plotted since those figures would look very similar to Figure 5 for the B_{AB} LF's. Essentially the same trends observed earlier for the B_{AB} LF's are seen for R_c and U as well, and our earlier discussion applies. We also find that the best-fit faint-end slopes α are independent of band. For all three galaxy types, the full range in best-fit α values is only about 0.2 among the three bands B_{AB} , R_c , and U . Thus, to convert the LF results from one band to another, it is a good approximation to keep α fixed and just apply an appropriate offset in M^* based on the mean rest-frame color for that galaxy type. Moreover, it also turns out that the evolution parameters Q and P agree well from band to band. In retrospect this is not surprising. We expect that Q should stay the same because our galaxy classification scheme is based on selecting galaxies of similar rest-frame colors at different redshifts. For example, however much the average M_B changes with redshift for our early-type galaxies, M_R for those same galaxies should change by about the same amount, since by definition, the rest-frame color $M_B - M_R$ of our early-type galaxies needs to stay about constant with redshift. Thus, for populations of similar rest-frame color, Q and subsequently P will be approximately independent of which band is chosen for the LF.

However, although the *rate* $P + Q$ of luminosity density evolution for a particular galaxy type

is similar in different bands, the *normalization* $\rho_L(z = 0)$ is in general different. This makes the overall evolution of ρ_L somewhat different for the different bands, and Figure 14 compares $\rho_L(z)$ for the three bands, including subdivision by galaxy type. For R_c and U , we have first applied AB corrections $R_{cAB} = R_c + 0.169$ and $U_{AB} = U + 0.69$ (Fukugita et al. 1995) before applying the same conversion we used for B_{AB} to convert to $h \text{ W Hz}^{-1} \text{ Mpc}^{-3}$ units (see end of § 3.2). The relative contribution of late-type galaxies is strongest for U and weakest for R_c , and vice versa for early-type galaxies, as expected. This causes the total ρ_L to increase with redshift at a somewhat faster rate in U than in R_c , but Figure 14 (upper left panel) shows that the difference is not very strong, at least over the CNOC2 redshift range.

4.3. SED Type Distributions, Number Counts, and Color Distributions

So far we have not explicitly needed the distribution of SED types, but in order to obtain the LF-computed galaxy number counts and color distributions, the SED type distribution will be helpful. Otherwise we will have to make some ad hoc assumptions, e.g., a uniform type distribution within each of the three galaxy categories, or delta functions at a number of characteristic SED types. We first define an overall fractional type distribution F in bins of SED type t by

$$F(t_1 < t < t_2) \equiv \sum_{t_1 < t_i < t_2} W_i/S_j(z_i) \bigg/ \sum_{\text{all galaxies}} W_i/S_j(z_i) \quad (21)$$

Here we are weighting by the usual statistical weights W_i , as well as by the appropriate selection function $S_j(z_i)$ from equation (15), where $j = \text{early, intermediate, or late}$ indicates the category to which galaxy i belongs. The inverse selection function weighting corrects $F(t)$ to what one would obtain for a volume-limited sample with $-22 < M_{B_{AB}} - 5 \log h < -16$, and there is also an implicit assumption that the LF is independent of SED type t *within* each of the three galaxy categories. Also, because the LF evolves, $F(t)$ will change with redshift, but for illustrative purposes we will neglect this complication and simply plot in Figure 15 the $F(t)$ computed over the full redshift completeness range $0.12 < z < 0.55$. In our number count and color distribution calculations we actually only need the fractional distribution $G_j(t)$ *within* each of the three galaxy categories j :

$$G_j(t_1 < t < t_2) \equiv \sum_{t_1 < t_i < t_2 \cap \text{galaxy } i \text{ in category } j} W_i/S_j(z_i) \bigg/ \sum_{\text{all galaxies in category } j} W_i/S_j(z_i) \quad (22)$$

We have explicitly checked that G_j changes only weakly with redshift, so that it is a good approximation to adopt the G_j computed for the full redshift range $0.12 < z < 0.55$ in our subsequent calculations. Note that the appearance of the histogram in Figure 15 (the presence of peaks and valleys, how smooth or not it appears) may depend to some extent upon the choice of the set of original SED’s used to define the classification scheme.

We now consider the CNOC2 photometric sample with $R_c < 21.5$, the nominal spectroscopic limit. The galaxy number counts in the $UBVR_cI_c$ bands for this sample are plotted in Figure 16.

Note the turnover at faint magnitudes in the $UBVI_c$ bands is due to our explicit $R_c < 21.5$ cut and is *not* a result of incompleteness in the photometry in these bands. We also plot the number counts computed using the evolving B_{AB} -band LF's $\phi_j(M, z)$ and the fractional distributions $G_j(t)$ derived previously. In particular, galaxies with redshifts $z_1 < z < z_2$ will contribute to the number counts N in an apparent magnitude interval $m_1 < m < m_2$ of a particular band according to

$$N(m_1 < m < m_2; z_1 < z < z_2) = \sum_j \sum_t G_j(t) \int_{z_1}^{z_2} \left(\frac{dV}{dz} \right) dz \int_{M_{\min}(z, m_1, t)}^{M_{\max}(z, m_2, t)} \phi_j(M, z) dM, \quad (23)$$

where $M_{\min}(z, m_1, t)$ and $M_{\max}(z, m_2, t)$ are the absolute magnitude limits observable at redshift z , given the apparent magnitude limits m_1 and m_2 and the k -corrections connecting absolute B_{AB} magnitudes to the apparent magnitudes for the band in question. These k -corrections depend on the galaxy type t and are calculated using our usual CWW SED's. Also, in the second sum above, G_j is evaluated using bins of width $\Delta t = 0.2$ (as in Figure 15). We calculate N first considering only the contribution of galaxies with $0.12 < z < 0.55$, the nominal redshift completeness range adopted for the LF analysis. We can clearly see the shortfall compared to the actual counts at both bright and faint magnitudes, resulting from neglect of low- and high- z galaxies, respectively. The match between the observed and LF-computed counts is much improved by extending the redshift range to $0 < z < 0.75$, and further extension to $0 < z < 1$ makes little difference. The good agreement seen is *not* a circular result, since the LF is fit only for galaxies within $0.12 < z < 0.55$, so that including the LF-*extrapolated* contribution from galaxies outside that redshift range serves as an independent check on the validity of our LF and evolution models.

We then repeat the same exercise but using various color distributions, as shown in Figure 17. The LF-computed color distributions are calculated using an expression analogous to equation (23), but augmented with the appropriate limits in the observed colors. The LF-computed results again converge by $z = 0.75$ and the match to the observed color distributions is good for all four colors shown: $B - R_c$, $R_c - I_c$, $V - R_c$, and $U - R_c$. (We should recall here that we did adjust the CWW SED I_c magnitudes to improve the match to the $R_c - I_c$ distribution, as mentioned in § 3.1). The overall reasonable agreement between the $0 < z < 1$ LF-computed color distributions and the observed distributions provides further validation of our evolving LF model and of our magnitude- and color-dependent weighting scheme defined back in § 2.1.

4.4. Potential Systematic Effects

Here we will consider a number of potentially important systematic sources of error which may affect our LF and evolution fits, specifically: (1) differences between the 0223 and 0920 patches; (2) random photometric errors; (3) potential redshift incompleteness; and (4) potential apparent magnitude incompleteness. We will find that typically our LF and evolution parameters are biased at less than the 1σ level.

4.4.1. Patch-to-Patch Variation

Since there are large-scale density fluctuations in our survey (Figure 6), we should check how well our results for the 0223 and 0920 patches agree. We do so in some detail, comparing the M^* - α (Figure 7) and P - Q error contours, as well as the trend of $\rho_L(z)$ by galaxy type. Encouragingly, the LF parameters M^* , α , P , and Q for the two patches are all consistent within their respective 2σ error contours. Examination of the $\rho_L(z)$ comparison shows excellent agreement of the LF-computed luminosity density evolution trends for all three galaxy types, despite the obvious density fluctuations seen in both patches.

4.4.2. Random Photometric Errors

Random photometric errors will in general cause an Eddington-type effect on the LF, such that M^* is biased brighter and α is biased steeper (see EEP). This effect is appreciable for photographic-plate-based surveys with magnitude errors $\sigma_m \sim 0.3$ mag (e.g., Loveday et al. 1992; Marzke et al. 1994b), but is essentially negligible for CCD-based surveys with magnitude errors $\sigma_m \sim 0.1$ mag (e.g., Lin et al. 1996a), though one can correct for it nonetheless by taking the LF to be a Schechter function *convolved* with a Gaussian magnitude error distribution with dispersion σ_m (see EEP). For CNOC2, $\sigma_{R_c} < 0.1$ mag at the nominal $R_c = 21.5$ spectroscopic limit and the consequent effects on M^* and α should be small. However, we should also confirm that the impact of photometric errors are likewise negligible for the P and Q evolution parameters. Moreover, since our galaxy classifications (and consequent derivation of k -corrections and absolute magnitudes) also make use of the $UBVI_c$ magnitudes apart from just R_c , the photometric error distributions in these various bands will affect our derivation of the LF and evolution parameters in a complicated way. The median magnitude errors for our $R_c < 21.5$ galaxies are 0.04 mag for R_c and I_c , 0.05 mag for V , 0.08 mag for B , and 0.16 mag for U . One could estimate the potential biases by fitting the LF’s of Monte Carlo mock CNOC2 galaxy catalogs, generated using the best-fit type-dependent LF and evolution parameters of the real sample, combined with the appropriate photometric error distributions in each of the CNOC2 bands. We will however use a less complicated procedure, and simply see what happens if we artificially *increase* the photometric errors of the real CNOC2 sample. Specifically, for each photometric band of each galaxy, we modify the observed magnitude by adding a random magnitude error. The random magnitude error is drawn from a Gaussian distribution with zero mean, and with dispersion equal to the PPP-estimated magnitude error for that particular band and galaxy. The photometric errors appropriate for the modified magnitudes are thus $\sqrt{2}$ times the original estimated errors. We repeat this procedure five independent times for each galaxy in the full CNOC2 *photometric* sample, so we end up with a five-fold larger “error-boosted” sample. Galaxy classifications and statistical weights are then computed using the same procedure as for the original sample, but now based on the modified magnitudes, and we then re-fit for the LF and evolution parameters. The biases in the fitted parameters of the “error-boosted” sample relative to the original CNOC2 sample give us an estimate of the biases inherent in the CNOC2 sample

relative to a hypothetical sample with no photometric errors. Our “error-boosted” P and Q values are plotted as solid points in Figure 18 (upper left panel), and are within the 1σ error contours of the original P - Q values. Likewise, the “error-boosted” M^* and α values (not plotted) are also within about 1σ of the original values (but systematically biased bright or steep, as expected). We thus conclude that the existing photometric errors of our sample do not significantly bias our LF and evolution parameter fits.

4.4.3. Redshift Incompleteness

As described in § 2, our nominal redshift limits $z = 0.12$ and 0.55 are set by the observability of important absorption and emission features over the 4400-6300Å spectroscopic range. Examination of Figure 6 shows that, as expected, the observed (weighted) redshift distribution outside the $0.12 < z < 0.55$ range tends to lie low compared to the distribution from the best-fit LF model, although the effect is primarily seen for early and intermediate types at higher redshifts (compare also Figures 3 and 4). However, in the highest- z bin $0.5 < z < 0.55$ *within* our nominal redshift range, there is already a noticeable dip in the redshift distributions for early and intermediate galaxies. This perhaps indicates some unaccounted residual redshift incompleteness in that bin, and we should check what happens if we exclude that bin from our analysis. Also, we note that the $0.1 < z < 0.2$ bins may suffer from incompleteness in late-type galaxies, if $H\beta$ and [OIII] $\lambda\lambda 5007, 4959$ do not adequately pick up for the unobservable [OII] $\lambda 3727$ line.

Thus we redo our fits for the more redshift-complete range $0.2 < z < 0.5$, over which the most important redshift-identification features, Ca II H+K and [OII] $\lambda 3727$, are always observable. We in fact find M^* and α values to be in good agreement with the original ones, and as shown in Figure 18 (top right panel), the P and Q parameters agree within $\lesssim 1.5\sigma$ of the original values. It thus appears that our LF parameters are not significantly biased by any residual redshift incompleteness effects, even though there are some possible hints of incompleteness in the $0.5 < z < 0.55$ bin for early- and intermediate-type galaxies.

4.4.4. Apparent Magnitude Incompleteness

As shown in Figure 1 and discussed in § 2.1, the (uncorrected) raw differential redshift success rate at the nominal spectroscopic limit $R_c = 21.5$ is 0.5, and the redshift sampling rate is 0.2 so that the typical galaxy weight is about 5. Here we check if using a 0.5 mag brighter limit of $R_c = 21.0$, where there is an improved raw redshift success rate of 0.6 and a smaller typical galaxy weight of about 2, will make a significant difference in the LF evolution results. Figure 18 (bottom left) shows that the P and Q values for the $17.0 < R_c < 21.0$ sample are always within the original 1σ contours. Likewise, the M^* and α values are within the original 2σ contours. We thus conclude that potential unaccounted incompleteness over the $21.0 < R_c < 21.5$ magnitude range does not

make a significant difference to our results.

4.5. *B*-band Selection

Here we examine the effects of using a *B*-selected CNOC2 sample compared to our usual R_c -selected sample. We do this partly in anticipation of our later comparison with the *B*-selected Autofib Redshift Survey in § 5.3. We define a $18 < B < 23$ CNOC2 sample ($N = 1936$) and compute new weights, using the bound $|B_i - B_j| \leq 0.25$ in place of the corresponding R_c bound in equation (3). The *B*-selected *P*-*Q* results are shown in Figure 18 (bottom right panel), where we find agreement within 2σ with the R_c -selected results, except for the early-type galaxies, which now show weak *positive* density evolution $P = 0.6$. In general the *B*-selected sample shows more positive density evolution compared to the R_c -selected sample, but the luminosity evolution parameters *Q* are very similar. The corresponding M^* and α values agree well within 1σ for the early and intermediate types, and are within 2σ for the late types. We thus conclude that the *B*- and R_c -selected samples do give LF evolution results that are generally in good agreement, with the sole exception of the *P* value for the early types.

5. Comparisons with Previous Surveys

In this section we compare our LF evolution results with those obtained from three previous intermediate-*z* redshift surveys. We first briefly compare against the field galaxy sample from the CNOC1 Cluster Redshift Survey, the immediate predecessor of CNOC2. We then continue with the two next largest intermediate-*z* redshift survey samples, specifically the Canada-France Redshift Survey and the composite Autofib Redshift Survey.

5.1. CNOC1 Cluster Redshift Survey — Field Sample

The CNOC1 Cluster Redshift Survey (Carlberg et al. 1996; Yee et al. 1996) included observations of both cluster and field galaxies in the fields of 16 high X-ray luminosity clusters. The observational techniques used in the CNOC1 survey are very similar to those used in CNOC2, but CNOC1 galaxies only have Gunn *r* and *g* photometry available. Lin et al. (1997) examine the LF for a sample of 389 CNOC1 field galaxies, with redshifts $0.2 < z < 0.6$ and apparent magnitudes $18 < r < 22$. Non-evolving luminosity functions in B_{AB} and Gunn *r* are computed, for the whole CNOC1 field sample, as well as for blue and red subsets divided by the observed $g - r$ color of a CWW Sbc galaxy. Consistent with the CNOC2 results, the CNOC1 LF's show the same trend of a steeper faint-end slope for blue galaxies relative to red ones. The CNOC1 sample is too small for the LF evolution analysis of the present paper, but Lin et al. (1997) have computed luminosity densities and have shown that the CNOC1 blue galaxy $\rho_L(z)$ increases strongly with redshift, while

the CNOC1 red galaxy $\rho_L(z)$ is essentially constant with z . These results are consistent with those found for the CNOC2 sample.

We have also computed non-evolving B_{AB} and r LF’s for CNOC2 galaxies, using basically the same CWW Sbc cut applied to CNOC1. For each of the all, blue, and red samples and for both rest-frame bandpasses, we confirm that the CNOC1 and CNOC2 results are indeed in good quantitative agreement in M^* , α , and normalization. The errors of the CNOC1 LF’s are fairly large, however, primarily because of its much smaller sample size, so that unfortunately little improvement in the LF constraints is gained by adding the CNOC1 field data into the CNOC2 sample. The present CNOC2 LF results essentially supercede those obtained earlier from CNOC1.

5.2. Canada-France Redshift Survey (CFRS)

The Canada-France Redshift Survey (CFRS; Lilly et al. 1995a) consists of 591 galaxy redshifts up to $z \sim 1$. The sample is selected in the I -band with $17.5 \leq I_{AB} \leq 22.5$, and is distributed over five widely separated fields, totaling 125 arcmin^2 on the sky. Lilly et al. (1995b) examine the evolution of the CFRS LF for $0 \lesssim z \lesssim 1$. They divide their sample by observed $(V - I)_{AB}$ color, also using CWW SED’s, and find rapid evolution in the LF of galaxies bluer than a CWW Sbc galaxy, contrasted with little change in the LF of redder-than-Sbc galaxies.

Lilly et al. (1995b) also split their sample into several redshift bins, including 208 galaxies in a $0.2 < z < 0.5$ bin which overlaps most with the CNOC2 redshift limits. In Figure 19, we compare the CFRS B_{AB} LF results (the “best” estimates of Lilly et al. 1995b) against those for a nearly ten times larger sample of 1842 CNOC2 galaxies with $0.2 < z < 0.5$. We also use the CWW Sbc cut to divide our sample into red and blue subsets; we initially do *not* include evolution, as the CFRS results are fit using non-evolving Schechter functions. The bottom panels in the figure show that the M^* - α values for the two surveys are in good agreement (the CFRS error contours have been calculated by us using CFRS redshift catalog data kindly supplied by Simon Lilly). This is also demonstrated in the middle panels, where we have renormalized the CNOC2 LF’s to match the normalizations of the CFRS LF’s, using an equation analogous to equation (20), in order to focus on comparing the LF shapes. The renormalizations affect the red-galaxy LF’s very little, as the CNOC2 and CFRS results agree well in the first place. However, as shown in the top panels, there is a noticeable difference in the blue-galaxy LF’s, where CNOC2 shows a higher number density than CFRS.

We next add evolution into our CNOC2 LF fits, using our usual 5-parameter method, in order to extrapolate our luminosity density results into the $0.5 < z < 1$ redshift range probed by CFRS, as shown in Figure 20. We have extended the upper redshift limit to $z = 0.65$ for the CNOC2 blue sample, in order have an additional data point to show. Notice from Figure 3 that there does not appear to be any obvious incompleteness for bluer-than-Sbc CNOC2 galaxies for $0.55 < z < 0.65$ (as there is for redder-than-Sbc galaxies), and also note that there is no obvious

dip due to incompleteness in the last CNOC2 blue-galaxy ρ_L point at $z \approx 0.6$ in Figure 20. The CFRS ρ_L results are taken from Lilly et al. (1996; their “LF-estimated” 4400Å values), and the two surveys do appear consistent within the errors. The CNOC2 blue $\rho_L(z)$ and extrapolation more or less parallel the CFRS results, but are about 50% higher overall. The CNOC2 red $\rho_L(z)$ and extrapolation agree well with CFRS at $z \lesssim 0.7$, but appears to overshoot CFRS in the highest redshift bin, $z \sim 0.9$.

We note that the difference in the CNOC2 and CFRS blue-galaxy luminosity densities may be consistent with the galaxy density fluctuations expected for these two surveys. We estimate (using the procedure described at the end of § 3.2) that the density fluctuations $\delta\rho/\rho$ are approximately 12% and 13% for the $0.2 < z < 0.5$ volumes in CNOC2 and CFRS, respectively. The ratio of roughly 1.5 in the blue-galaxy ρ_L for the two surveys would then have a 1σ uncertainty (assuming Gaussian galaxy density fluctuations) of about ± 0.27 , so the luminosity densities differ at the $< 2\sigma$ level, and even less so if we include the remaining sampling and LF-fit contributions to the total error on ρ_L . On the other hand, it is unclear why we do not see any differences in the respective red galaxy populations, which should show stronger density fluctuations than the blue galaxies (e.g., Figure 6). Thus the blue-galaxy differences may be caused instead by some systematic differences in, e.g., galaxy classification and/or photometry for blue galaxies in the two surveys, although one might then have expected to see a more significant difference in the shapes of the CNOC2 and CFRS luminosity functions.

Recently, galaxy evolution results have also been reported for a sample of 341 galaxies drawn from the CFRS and the Autofib/Low Dispersion Survey Spectrograph (LDSS) data sets, which have morphologies classified from Hubble Space Telescope images (Brinchmann et al. 1998; Lilly et al. 1998). Though there is clearly correlation between the early, intermediate, and late SED/color classifications adopted in this paper and the “elliptical,” “spiral,” and “peculiar” morphological categories, respectively, defined by Brinchmann et al. (1998), the correlations are broad enough to preclude a detailed quantitative comparison. We will defer this for a future paper on morphological classifications of CNOC2 galaxies. Here we will simply mention two LF-related results from Brinchmann et al. (1998) which are qualitatively consistent with our results: (1) the LF of the spiral CFRS/LDSS sample indicates about 1 magnitude of luminosity evolution in B_{AB} by $z \simeq 1$, similar to the $Q = 0.9$ value we find for the CNOC2 intermediate-type galaxies, which should be dominated by spirals; and (2) the peculiar/irregular CFRS/LDSS galaxies appear to be primarily responsible for the rapid rise with redshift of the blue galaxy luminosity density, a result consistent with our observation that late-type CNOC2 galaxies cause the strong observed increase in the overall ρ_L with redshift.

5.3. Autofib Redshift Survey

The Autofib Redshift Survey is a composite of various galaxy survey samples (Ellis et al. 1996 and references therein) and contains over 1700 redshifts with $0 < z \lesssim 0.75$. The survey is selected in

the blue, with apparent magnitudes in the range $11.5 < b_J < 24.0$. Ellis et al. (1996) find an overall steepening of the LF at higher redshifts, and similar to CNOC2 and CFRS, the LF evolution is dominated by late-type galaxies, which also show increased [OII] $\lambda 3727$ emission and thus stronger star formation at higher redshifts.

Ellis et al. (1996) give overall b_J LF's in several redshift intervals, including $0.15 < z < 0.35$ and $0.35 < z < 0.75$ bins which overlap with CNOC2. In Figure 21, we make the same redshift cuts (but with a $z = 0.55$ upper limit), and compute non-evolving LF's for comparison. We show results both for the standard CNOC2 $17 < R_c < 21.5$ sample ($N = 2076$; *filled triangles*) and for a blue-selected $18 < B < 23$ CNOC2 sample ($N = 1830$; *filled squares*). There is a significant systematic difference between the two CNOC2 samples, where the B -selected sample shows a steeper α and brighter M^* , because of the increased contribution (due to k -correction effects) of bluer late-type galaxies in the B -selected sample. However, this systematic offset between the R_c - and B -selected samples is an artifact of trying to force fit a single LF to the full galaxy population, and does not occur if we subdivide into three populations as we did before (§ 4.5). Using a B -selected CNOC2 sample significantly improves the agreement with the $0.15 < z < 0.35$ Autofib results, although the 2σ M^* - α error contours still do not quite overlap, as Autofib shows a steeper α and a brighter M^* . (Note that although the CNOC2 and Autofib samples here are similar in size, the Autofib error contours are smaller because of Autofib's much wider *apparent* magnitude limits compared to CNOC2.) Nonetheless, a visual comparison of the two lower- z LF's (top left panel of Figure 21) does show reasonable agreement. However, in the higher- z bin there is a noticeable mismatch in M^* and/or normalization between the CNOC2 and Autofib results.

The causes of these discrepancies are not known, but can include sampling fluctuations, as well as unaccounted systematic differences in sample selection, galaxy classifications and k -corrections, photometry, and the like (see Lin et al. 1997 for additional discussion). Note that sample size may be an important consideration for the comparison in the higher-redshift bin. Though the overall Autofib sample contains some 1700 redshifts, the relevant sample sizes here are smaller (Ellis 1997, Figure 6b): $N = 665$ for $0.15 < z < 0.35$ and only $N = 152$ for $0.35 < z < 0.75$. The corresponding CNOC2 (B -selected) sample sizes are $N = 940$ and $N = 890$, so that the high- z CNOC2 sample is nearly 6 times larger than the corresponding Autofib data set. Also, large-scale galaxy density fluctuations may play a role. The values of $\delta\rho/\rho$ are estimated to be 16% and 13% for the low- and high- z CNOC2 volumes, respectively, and are presumably somewhat larger for the corresponding Autofib volumes (although we have not done the exact calculations as we lack certain needed Autofib sample details). As we saw earlier in our CFRS comparison, such values of $\delta\rho/\rho$ do not preclude a factor of 1.5 in the relative LF normalizations, which would significantly reduce the discrepancy in the high- z bin. We have also checked whether random k -correction errors and photometric errors in the Autofib sample might be responsible for the M^* and α differences. The Autofib k -corrections are assigned primarily on the basis of galaxy spectral classifications, rather than more directly via multicolor photometry as we do. Ellis et al. (1996) estimate that their k -correction errors due to spectral misclassifications have a redshift dependence $\sigma_B \sim 0.5z$ mag (our

interpretation of their Figure 6). Also, the Autofib photometry is based mainly on photographic plate data with errors typically 0.1-0.2 mag, in contrast to CNOC2 CCD photometry with errors < 0.1 mag. Both these effects will tend to bias the Autofib results to brighter M^* and steeper α (see § 4.4.2), so we have checked the effect of adding such k -correction errors and photometric errors (0.2 mag Gaussian) to our B magnitudes. In agreement with Ellis et al. (1996) and Heyl et al. (1997), we find that the differences are small, with $|\Delta M^*| \lesssim 0.2$ and $|\Delta\alpha| \lesssim 0.1$, not enough to significantly improve the agreement of the M^* - α contours in the low- z bin, and of the wrong sign for the high- z bin. We have also tried computing b_J absolute magnitudes and LF's for CNOC2 galaxies using the b_J response function (instead of our usual Johnson B) but it makes negligible difference to our results. Additional exploration of Autofib vs. CNOC2 photometry systematics likely requires us to apply our photometry codes to the original Autofib data. Such a detailed comparison may not be warranted given that the main CNOC2/Autofib differences lie in the high- z bin, where the main culprits may very well be galaxy density fluctuations and the small Autofib sample size there.

Heyl et al. (1997) have classified Autofib galaxies into six types based on cross-correlation against local galaxy spectral templates, and examined the evolution of the LF divided by galaxy spectral type. Note that in discussing LF evolution, Heyl et al. typically use the three broader categories “early-type E/S0,” “early-type spirals,” and “late-type spirals” (each including two of their original six types), which have obvious but broad correlations relative to our early, intermediate, and late types, respectively. Also, their LF evolution model is similar but not identical to ours, and involves six parameters compared to our five, with the additional parameter characterizing the rate of evolution of α , which we have taken as fixed with redshift. In addition, unlike our analysis, Heyl et al. do not plot error contours, like our P - Q diagrams, to show the correlations among their LF evolution parameters. Because both their classification and analysis methods are different from ours, and because we have already noted some discrepancies between the CNOC2 and Autofib results above, we will not attempt a detailed quantitative comparison here. We will note however, that generally speaking the Heyl et al. (1997) results are qualitatively consistent with ours. Specifically, they find: (1) no significant evolution of the E/S0 LF out to at least $z \sim 0.5$; (2) modest evolution in the LF of early-type spirals, characterized by steepening of α at higher redshifts rather than by changes in M^* or ϕ^* ; and (3) strong evolution in the LF of late-type spirals, described by steepening α , brightening M^* , and increasing ϕ^* at higher z . The main difference compared to CNOC2 lies in the steepening α observed in Autofib, contrasted with the good match of our $\alpha(z) = \text{constant}$ models to the CNOC2 data (see Figure 8 in particular). Also, the $Q \approx 1$ luminosity evolution we find in our early- and intermediate-type LF's is somewhat different from the trends seen in the Autofib E/S0 and early-spiral LF's. It is not clear at present what is responsible for these detailed CNOC2/Autofib evolution differences, but we note in particular that the different galaxy classification schemes involved may play an important role. We will return to this comparison again in a future paper on application of spectral classifications to the full CNOC2 sample.

6. Conclusions

In this paper we have examined the evolution of the luminosity function for a sample of over 2000 field galaxies, with $0.12 < z < 0.55$ and $17.0 < R_c < 21.5$, drawn from two different sky patches of the CNOC2 Field Galaxy Redshift Survey. Although this sample comprises only half the ultimate CNOC2 data set, it is nonetheless the largest intermediate-redshift galaxy survey sample at present. The availability of $UBVR_cI_c$ photometry for our sample allows galaxy classifications by SED type, as well as computation of LF’s in different rest-frame bandpasses. In addition, the multicolor photometry permits us to examine sample selection effects in detail, and allows us to construct galaxy weights to account for our redshift success rates as functions of galaxy magnitude and color.

In particular, we have calculated LF parameters in the B_{AB} , R_c , and U bands for early-, intermediate-, and late-type galaxies, classified using $UBVR_cI_c$ colors derived from the non-evolving galaxy spectral energy distributions of Coleman, Wu, & Weedman (1980). We present a description of the LF evolution in terms of a five-parameter model involving the usual three Schechter function parameters, plus two additional parameters P and Q describing number density and luminosity evolution rates, respectively (eq. 10). The best-fit parameters of our LF evolution models are given in Tables 1 and 2. We find that the faint-end slope of the LF is steeper for later-type galaxies relative to earlier-type objects, consistent with previous LF studies at both intermediate and low redshifts.

The principal results of this paper are the quantitative separation of luminosity and density evolution in the LF’s of different galaxy populations, and the finding that the character of the LF evolution is strongly type dependent, varying from primarily luminosity evolution for early-type galaxies to predominantly density evolution for late-type objects. We quantify the rates of luminosity function evolution using our P and Q parameters. Specifically, we see that (for $q_0 = 0.5$): (1) the late-type galaxy LF is best fit by strong positive density evolution ($P = 3.1$), with nearly no luminosity evolution ($Q = 0.2$); (2) the intermediate-type LF shows positive luminosity evolution ($Q = 0.9$) plus weak positive density evolution ($P = 0.7$), resulting in mild positive evolution in the luminosity density ρ_L ; and (3) the early-type LF shows positive luminosity evolution ($Q = 1.6$) which is nearly compensated by negative density evolution ($P = -1.1$), resulting in a very weak positive evolution in ρ_L . However, we should note that the P and Q parameters are strongly correlated for late-type galaxies, and “no-evolution” for early- and intermediate-type objects is ruled out at only about the 2σ confidence level. Nonetheless, it is a robust result that the LF’s of late and early+intermediate galaxies are evolving differently and occupy different regions of P - Q parameter space. Moreover, there is a distinct contrast between the sharply rising luminosity density of late-type galaxies and the relatively constant ρ_L of early- and intermediate-type objects. (This is probably not too surprising given that one expects the rapidly evolving population to consist of those galaxies actively forming stars in the past, which are essentially the late types.) These general conclusions are little changed by adopting a different value of $q_0 = 0.1$.

The rates of luminosity evolution ($Q \approx 1$) for our early and intermediate types are in the range expected from models of galaxy evolution (e.g., Bruzual & Charlot 1996). At face value, the strong density evolution observed for late types suggests that mergers play an important role in the evolution of these galaxies. However, other processes, particularly those affecting star formation properties, may mimic the effect of mergers and cause similar changes in number density (e.g., a starbursting sub-population among the late types at high- z may be responsible for the density evolution). In Paper II, we will test various physical galaxy evolution models in detail, including the effects of different star formation histories, ages, stellar initial mass functions, dust content, and the like. Nonetheless, whatever the responsible physical mechanisms are, they will need to explain the strong correlation between galaxy type and the character of the LF evolution, in particular the strong increase in the apparent density evolution as one proceeds to later galaxy types. The relevant underlying physical variables controlling the evolution should thus be closely correlated with the galaxy SED type. On the other hand, within each of our galaxy categories, those physical variables are probably not strongly correlated with galaxy luminosity, since the data are well-fit by our fixed- α evolution models (so that the evolution does not vary much with luminosity within each galaxy category). It may be a challenge for physical models to explain this combination of strong type-dependence in the LF evolution, coupled with relatively little luminosity-dependence of the evolution within each galaxy type.

We also compute SED type distributions, $UBVR_cI_c$ galaxy number counts, and various color distributions for CNOC2 galaxies. In particular, we find that extrapolations of our LF evolution models to $z \approx 0.75$ yield good matches to the observed number counts and color distributions, thus providing an additional check on the validity of our LF evolution results. In addition, we have verified that various systematic effects, specifically patch-to-patch variations, photometric errors, surface brightness selection, redshift incompleteness, and apparent magnitude incompleteness, do not significantly affect our results ($\lesssim 1\sigma$ difference typically).

Finally, we note that our LF results are generally consistent with those found in previous intermediate- z redshift surveys, as verified in specific comparisons against results from the next two largest samples, CFRS and Autofib. However, there are still some unresolved detailed discrepancies, particularly with respect to the B -selected Autofib survey, which may be due to differences in galaxy classification or sample selection methods.

In this paper, we have simply presented a *description* of the evolution of the LF's of different intermediate-redshift galaxies, without delving into the possible underlying physical processes. As mentioned earlier, in our second LF paper we will actually confront the CNOC2 observations against various galaxy evolution models, in order to better understand and constrain those physical mechanisms. Subsequent papers on galaxy population evolution in CNOC2 will also make use of the morphological and spectral information that will become available for CNOC2 galaxies once the appropriate data are fully reduced. Ultimately the doubled size of the full CNOC2 sample over the present interim sample will significantly improve upon the LF evolution constraints that we have presented here. We are also in the process of deriving properly calibrated photometric redshifts,

which should provide another factor of two increase in useful sample size for $R_c < 21.5$ galaxies. Future papers will re-examine the question of LF evolution using these even larger CNOC2 galaxy data sets.

The CNOC project is supported in part by a Collaborative Program grant from the Natural Sciences and Engineering Research Council of Canada (NSERC). HL acknowledges support provided by NASA through Hubble Fellowship grant #HF-01110.01-98A awarded by the Space Telescope Science Institute, which is operated by the Association of Universities for Research in Astronomy, Inc., for NASA under contract NAS 5-26555. HY and RC wish to acknowledge support from NSERC operating grants. Thanks also to Pat Hall for a careful reading of the manuscript and for providing useful comments and suggestions. Thanks in addition to Simon Lilly and Matthew Colless for kindly providing CFRS and Autofib data, respectively. Finally, we wish to thank CTAC of CFHT for the generous allotment of telescope time, as well as to acknowledge the fine support received from CFHT staff.

REFERENCES

- Barrow, J. D., Bhavsar, S. P., & Sonoda, D. M. 1984, MNRAS, 210, 19p
- Baugh, C., Cole, S., Frenk, C. S., & Lacey, C. G. 1998, ApJ, 498, 504
- Bessel, M. S. 1990, PASP, 102, 1181
- Brinchmann, J., et al. 1998, ApJ, 499, 112
- Bromley, B. C., Press, W. H., Lin, H., & Kirshner, R. P. 1998, ApJ, 505, 25
- Bruzual A., G., & Charlot, S. 1996, in preparation
- Buser, R., & Kurucz, R. L. 1978, A&A, 70, 555
- Cardelli, J. A., Clayton, G. C., & Mathis, J. S. 1989, ApJ, 345, 245
- Carlberg, R., Yee, H. K. C., Ellingson, E., Abraham, R., Gravel, P., Morris, S., & Pritchet, C. J. 1996, ApJ, 462, 32
- Cole, S., Aragón-Salamanca, A., Frenk, C. S., Navarro, J. F., & Zepf, S. E. 1994, MNRAS, 271, 781
- Coleman, G. D., Wu, C.-C., & Weedman, D. W. 1980, ApJS, 43, 393 (CWW)
- Colless, M. 1998, to appear in Phil. Trans. R. Soc. Lond. A, preprint astro-ph/9804079
- Connolly, A. J., Csabai, I., Szalay, A. S., Koo, D. C., Kron, R. C., & Munn, J. A. 1995, AJ, 110, 2655

- Cowie, L. L., Songaila, A., Hu, E. M., & Cohen, J. G. 1996, *AJ*, 112, 839
- Crampton, D., Le Fèvre, O., Lilly, S. J., & Hammer, F. 1995, *ApJ*, 455, 96
- da Costa, L. N., et al. 1994, *ApJ*, 424, L1
- Dalcanton, J. J. 1998, *ApJ*, 495, 251
- de Lapparent, V., Galaz, G., Arnouts, S., Bardelli, S., & Ramella, M. 1997, *ESO Messenger*, 89, 21
- Efstathiou, G., Ellis, R. S., & Peterson, B. A. 1988, *MNRAS*, 232, 431 (EEP)
- Ellis, R. S. 1997, *ARA&A*, 35, 389
- Ellis, R. S., Colless, M., Broadhurst, T., Heyl, J., & Glazebrook, K. 1996, *MNRAS*, 280, 235
- Ferguson, H. C., & McGaugh, S. S. 1995, *ApJ*, 440, 470
- Fisher, K. B., Strauss, M. A., Davis, M., Yahil, A., & Huchra, J. P. 1992, *ApJ*, 389, 188
- Freeman, K. 1970, *ApJ*, 160, 811
- Fukugita, M., Shimasaku, K., & Ichikawa, T. 1995, *PASP*, 107, 945
- Geller, M. J., et al. 1997, *AJ*, 114, 2205
- Heyl, J., Colless, M., Ellis, R. S., & Broadhurst, T. 1997, *MNRAS*, 285, 613
- Hogg, D. W., Cohen, J. G., Blandford, R., & Pahre, M. A. 1998, *ApJ*, 504, 622
- Impey, C., & Bothun, G. 1997, *ARA&A*, 35, 267
- Kauffmann, G., Nusser, A., & Steinmetz, M. 1997, *MNRAS*, 286, 795
- Koo, D. C. 1985, *AJ*, 90, 418
- Koo, D. C., & Kron, R. G. 1992, *ARA&A*, 30, 613
- Lilly, S. J., et al. 1998, *ApJ*, 500, 75
- Lilly, S. J., Le Fèvre, O., Crampton, D., Hammer, F., & Tresse, L. 1995a, *ApJ*, 455, 50
- Lilly, S. J., Le Fèvre, O., Hammer, F., & Crampton, D. 1996, *ApJ*, 460, L1
- Lilly, S. J., Tresse, L., Hammer, F., Crampton, D., & Le Fèvre, O. 1995b, *ApJ*, 455, 108
- Lin, H., Kirshner, R. P., Shectman, S. A., Landy, S. D., Oemler, A., Tucker, D. L., & Schechter, P. L. 1996a, *ApJ*, 464, 60
- Lin, H., Kirshner, R. P., Shectman, S. A., Landy, S. D., Oemler, A., Tucker, D. L., & Schechter, P. L. 1996b, *ApJ*, 471, 617

- Lin, H., Yee, H. K. C., Carlberg, R. G., & Ellingson, E. 1997, *ApJ*, 475, 494
- Lin, H., Yee, H. K. C., Carlberg, R. G., Morris, S. L., et al. 1999, in preparation (Paper II)
- Liu, C. T., Green, R. F., Hall, P. B., & Osmer, P. S. 1998, *AJ*, 116, 1082
- Loveday, J., Peterson, B. A., Efstathiou, G., & Maddox, S. J. 1992, *ApJ*, 390, 338
- Marzke, R. O., & da Costa, L. N. 1997, *AJ*, 113, 185
- Marzke, R. O., da Costa, L. N., Pellegrini, P. S., Willmer, C. N. A., & Geller, M. J. 1998, *ApJ*, 503, 617
- Marzke, R. O., Geller, M. J., Huchra, J. P., & Corwin, H. G. 1994a, *AJ*, 108, 2
- Marzke, R. O., Huchra, J. P., & Geller, M. J. 1994b, *ApJ*, 428, 43
- Metcalfe, N., Ratcliffe, A., Shanks, T., & Fong, R. 1998, *MNRAS*, 294, 147
- O'Donnell, J. E. 1994, *ApJ*, 422, 158
- Oke, J. B. 1972, *ApJS*, 27, 21
- Ratcliffe, A., Shanks, T., Parker, Q. A., & Fong, R. 1998, *MNRAS*, 293, 197
- Sandage, A., Tammann, G. A., & Yahil, A. 1979, *ApJ*, 232, 352 (STY)
- Saunders, W., Rowan-Robinson, M., Lawrence, A., Efstathiou, G., Kaiser, N., Ellis, R. S., & Frenk, C. S. 1990, *MNRAS*, 242, 318
- Sawicki, M. J., Lin, H., & Yee, H. K. C. 1997, *AJ*, 113, 1
- Schechter, P. 1976, *ApJ*, 203, 297
- Schlegel, D. J., Finkbeiner, D. P., & Davis, M. 1998, *ApJ*, 500, 525
- Small, T. A., Sargent, W. L. W., & Hamilton, D. 1997, *ApJ*, 487, 512
- Sprayberry, D., Impey, C. D., Irwin, M. J., & Bothun, G. 1997, *ApJ*, 481, 104
- Yee, H. K. C. 1991, *PASP*, 103, 396
- Yee, H. K. C., Carlberg, R. G., Morris, S. L., et al. 1999, in preparation
- Yee, H. K. C., Ellingson, E., & Carlberg, R. G. 1996, *ApJS*, 102, 269 (YEC)
- Yee, H. K. C., et al. 1997, to appear in the proceedings of IAU Joint Discussion 11, Redshift Surveys in the 21st Century, ed. A. Fairall
- Zucca, E., et al. 1997, *A&A*, 326, 477

Table 1. B_{AB} LF Parameters ^a

Sample	N ^b	$M^*(z = 0.3)$ ^c	α	$\phi^*(z = 0)$ ^d	P	Q
$q_0 = 0.5$						
Early	611	-19.06 ± 0.12	0.08 ± 0.14	0.0203 ± 0.0036	-1.07 ± 0.49	1.58 ± 0.49
Intermediate	518	-19.38 ± 0.16	-0.53 ± 0.15	0.0090 ± 0.0023	0.73 ± 0.70	0.90 ± 0.72
Early+Inter.	1129	-19.19 ± 0.10	-0.20 ± 0.10	0.0291 ± 0.0049	-0.27 ± 0.40	1.29 ± 0.41
Late	1016	-19.26 ± 0.16	-1.23 ± 0.12	0.0072 ± 0.0033	3.08 ± 0.99	0.18 ± 0.71
$q_0 = 0.1$						
Early	611	-19.19 ± 0.12	0.08 ± 0.14	0.0197 ± 0.0036	-1.79 ± 0.49	2.00 ± 0.49
Intermediate	518	-19.51 ± 0.17	-0.53 ± 0.15	0.0087 ± 0.0023	0.00 ± 0.71	1.32 ± 0.72
Early+Inter.	1129	-19.32 ± 0.10	-0.20 ± 0.10	0.0284 ± 0.0048	-1.00 ± 0.40	1.72 ± 0.41
Late	1016	-19.38 ± 0.16	-1.23 ± 0.12	0.0071 ± 0.0034	2.34 ± 0.98	0.61 ± 0.71

^aAll tabulated errors are 1σ *one*-parameter errors. See Figures 7 and 9 for the joint *two*-parameter M^* - α and P - Q error contours, respectively.

^bWe apply apparent magnitude limits $17.0 < R_c < 21.5$, absolute magnitude limits $-22.0 < M_{B_{AB}} - 5 \log h < -16.0$, and redshift limits $0.12 < z < 0.55$ in defining our samples.

^cWe take Hubble constant $h = 1$.

^dUnits are $h^3 \text{ Mpc}^{-3} \text{ mag}^{-1}$.

Table 2. R_c and U LF Parameters ^a

Sample	N ^b	$M^*(z = 0.3)$ ^c	α	$\phi^*(z = 0)$ ^d	P	Q
		R_c	$q_0 = 0.5$			
Early	611	-20.50 ± 0.12	-0.07 ± 0.14	0.0185 ± 0.0037	-0.88 ± 0.52	1.24 ± 0.53
Intermediate	517	-20.47 ± 0.17	-0.61 ± 0.15	0.0080 ± 0.0023	0.89 ± 0.74	0.69 ± 0.76
Early+Inter.	1128	-20.61 ± 0.11	-0.44 ± 0.10	0.0230 ± 0.0046	0.08 ± 0.45	0.70 ± 0.48
Late	1012	-20.11 ± 0.18	-1.34 ± 0.12	0.0056 ± 0.0030	3.17 ± 1.03	0.11 ± 0.74
		R_c	$q_0 = 0.1$			
Early	609	-20.59 ± 0.12	-0.03 ± 0.14	0.0179 ± 0.0036	-1.54 ± 0.52	1.51 ± 0.53
Intermediate	518	-20.62 ± 0.18	-0.63 ± 0.15	0.0077 ± 0.0023	0.15 ± 0.75	1.11 ± 0.78
Early+Inter.	1127	-20.73 ± 0.11	-0.43 ± 0.10	0.0223 ± 0.0046	-0.59 ± 0.46	1.02 ± 0.48
Late	1012	-20.20 ± 0.17	-1.30 ± 0.12	0.0053 ± 0.0029	2.84 ± 1.06	0.22 ± 0.76
		U	$q_0 = 0.5$			
Early	611	-18.54 ± 0.11	0.14 ± 0.15	0.0213 ± 0.0036	-1.19 ± 0.48	1.85 ± 0.48
Intermediate	518	-19.27 ± 0.16	-0.51 ± 0.15	0.0092 ± 0.0026	0.68 ± 0.69	0.97 ± 0.70
Early+Inter.	1129	-18.92 ± 0.10	-0.22 ± 0.10	0.0302 ± 0.0051	-0.35 ± 0.40	1.40 ± 0.41
Late	1017	-19.32 ± 0.15	-1.14 ± 0.13	0.0095 ± 0.0039	2.67 ± 0.92	0.51 ± 0.66
		U	$q_0 = 0.1$			
Early	611	-18.67 ± 0.11	0.15 ± 0.15	0.0209 ± 0.0037	-1.93 ± 0.48	2.27 ± 0.48
Intermediate	518	-19.40 ± 0.16	-0.51 ± 0.15	0.0090 ± 0.0023	-0.05 ± 0.69	1.39 ± 0.71
Early+Inter.	1129	-19.05 ± 0.10	-0.22 ± 0.10	0.0294 ± 0.0049	-1.06 ± 0.40	1.82 ± 0.41
Late	1016	-19.44 ± 0.16	-1.13 ± 0.12	0.0087 ± 0.0038	2.29 ± 0.96	0.64 ± 0.68

^aAll tabulated errors are 1σ *one*-parameter errors.

^bWe apply apparent magnitude limits $17.0 < R_c < 21.5$, absolute magnitude limits $-23.0 < M_{R_c} - 5 \log h < -17.0$ or $-22.0 < M_U - 5 \log h < -16.0$, and redshift limits $0.12 < z < 0.55$ in defining our samples.

^cWe take Hubble constant $h = 1$.

^dUnits are $h^3 \text{ Mpc}^{-3} \text{ mag}^{-1}$.

Table 3. Luminosity Density Values ^a

Sample	$\rho_L(\text{fit}, z = 0)$	$\rho_L(0.12 < z < 0.25)$	$\rho_L(0.25 < z < 0.40)$	$\rho_L(0.40 < z < 0.55)$
	<i>B</i>	$q_0 = 0.5$		
Early	0.258 ± 0.042	0.301 ± 0.074	0.387 ± 0.071	0.265 ± 0.045
Intermediate	0.159 ± 0.028	0.217 ± 0.055	0.351 ± 0.063	0.259 ± 0.045
Late	0.189 ± 0.030	0.390 ± 0.094	0.580 ± 0.109	0.720 ± 0.123
Total	0.606 ± 0.078	0.907 ± 0.213	1.318 ± 0.230	1.244 ± 0.191
	<i>B</i>	$q_0 = 0.1$		
Early	0.252 ± 0.042	0.282 ± 0.072	0.360 ± 0.069	0.223 ± 0.040
Intermediate	0.155 ± 0.030	0.203 ± 0.053	0.317 ± 0.061	0.224 ± 0.040
Late	0.183 ± 0.030	0.364 ± 0.092	0.521 ± 0.106	0.615 ± 0.114
Total	0.591 ± 0.076	0.849 ± 0.208	1.197 ± 0.225	1.063 ± 0.177
	<i>R_c</i>	$q_0 = 0.5$		
Early	0.785 ± 0.130	0.896 ± 0.221	1.115 ± 0.202	0.750 ± 0.126
Intermediate	0.351 ± 0.066	0.472 ± 0.118	0.764 ± 0.139	0.565 ± 0.096
Late	0.320 ± 0.050	0.657 ± 0.158	1.012 ± 0.199	1.225 ± 0.215
Total	1.455 ± 0.186	2.024 ± 0.475	2.891 ± 0.510	2.539 ± 0.386
	<i>R_c</i>	$q_0 = 0.1$		
Early	0.778 ± 0.134	0.841 ± 0.217	1.006 ± 0.194	0.620 ± 0.112
Intermediate	0.346 ± 0.066	0.444 ± 0.116	0.692 ± 0.133	0.486 ± 0.088
Late	0.302 ± 0.050	0.604 ± 0.152	0.901 ± 0.187	1.055 ± 0.198
Total	1.426 ± 0.189	1.889 ± 0.463	2.599 ± 0.489	2.160 ± 0.356
	<i>U</i>	$q_0 = 0.5$		
Early	0.086 ± 0.014	0.102 ± 0.025	0.136 ± 0.024	0.092 ± 0.016
Intermediate	0.077 ± 0.014	0.106 ± 0.026	0.171 ± 0.031	0.127 ± 0.022
Late	0.118 ± 0.019	0.241 ± 0.057	0.344 ± 0.064	0.438 ± 0.076
Total	0.281 ± 0.036	0.449 ± 0.104	0.651 ± 0.114	0.657 ± 0.104
	<i>U</i>	$q_0 = 0.1$		
Early	0.084 ± 0.014	0.096 ± 0.025	0.123 ± 0.024	0.079 ± 0.014
Intermediate	0.075 ± 0.014	0.099 ± 0.026	0.154 ± 0.030	0.109 ± 0.020
Late	0.113 ± 0.019	0.224 ± 0.057	0.310 ± 0.062	0.381 ± 0.070
Total	0.273 ± 0.035	0.419 ± 0.103	0.587 ± 0.110	0.569 ± 0.096

^aUnits are $10^{20} h \text{ W Hz}^{-1} \text{ Mpc}^{-3}$. As discussed in the text, the tabulated 1σ errors include both bootstrap resampling errors (accounting for uncertainties in the LF fits and in galaxy sampling) and estimated uncertainties due to large-scale galaxy density fluctuations.

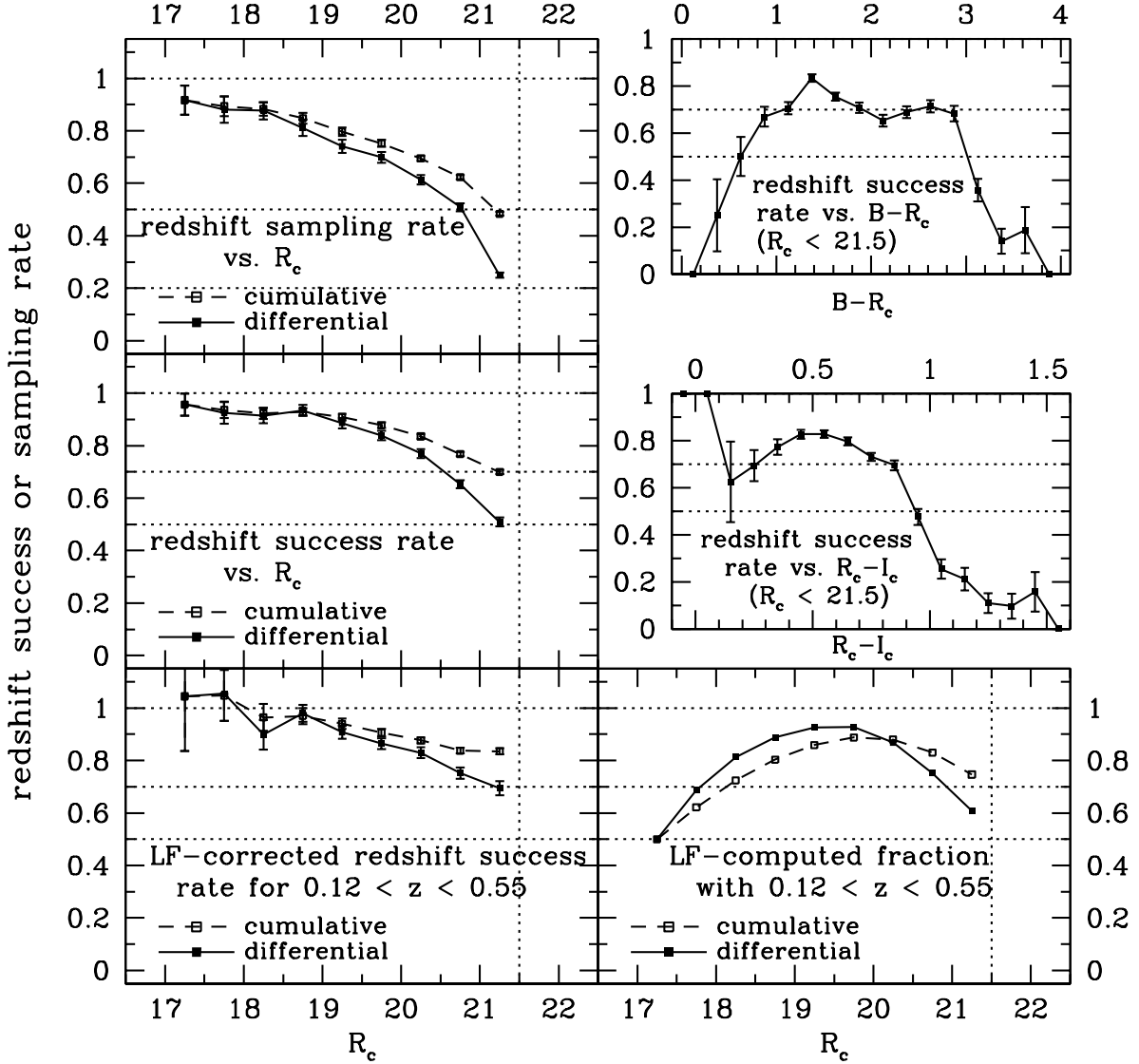


Fig. 1.— (Top left) Redshift sampling rate (fraction of *all* galaxies with redshifts) as a function of apparent magnitude R_c ; (middle left) redshift success rate (fraction of *spectroscopically observed* galaxies with redshifts) vs. R_c ; (top 2 panels on right) redshift success rate vs. $B - R_c$ and $R_c - I_c$ colors; (bottom right) fraction of all galaxies with $0.12 < z < 0.55$ as a function of R_c , computed from the best-fit evolving B_{AB} luminosity function derived in § 4.1; (bottom left) luminosity-function corrected redshift success rate vs. R_c , appropriate for galaxies within the nominal $0.12 < z < 0.55$ completeness limits (see discussion in text). All uncertainties are calculated assuming simple \sqrt{N} errors.

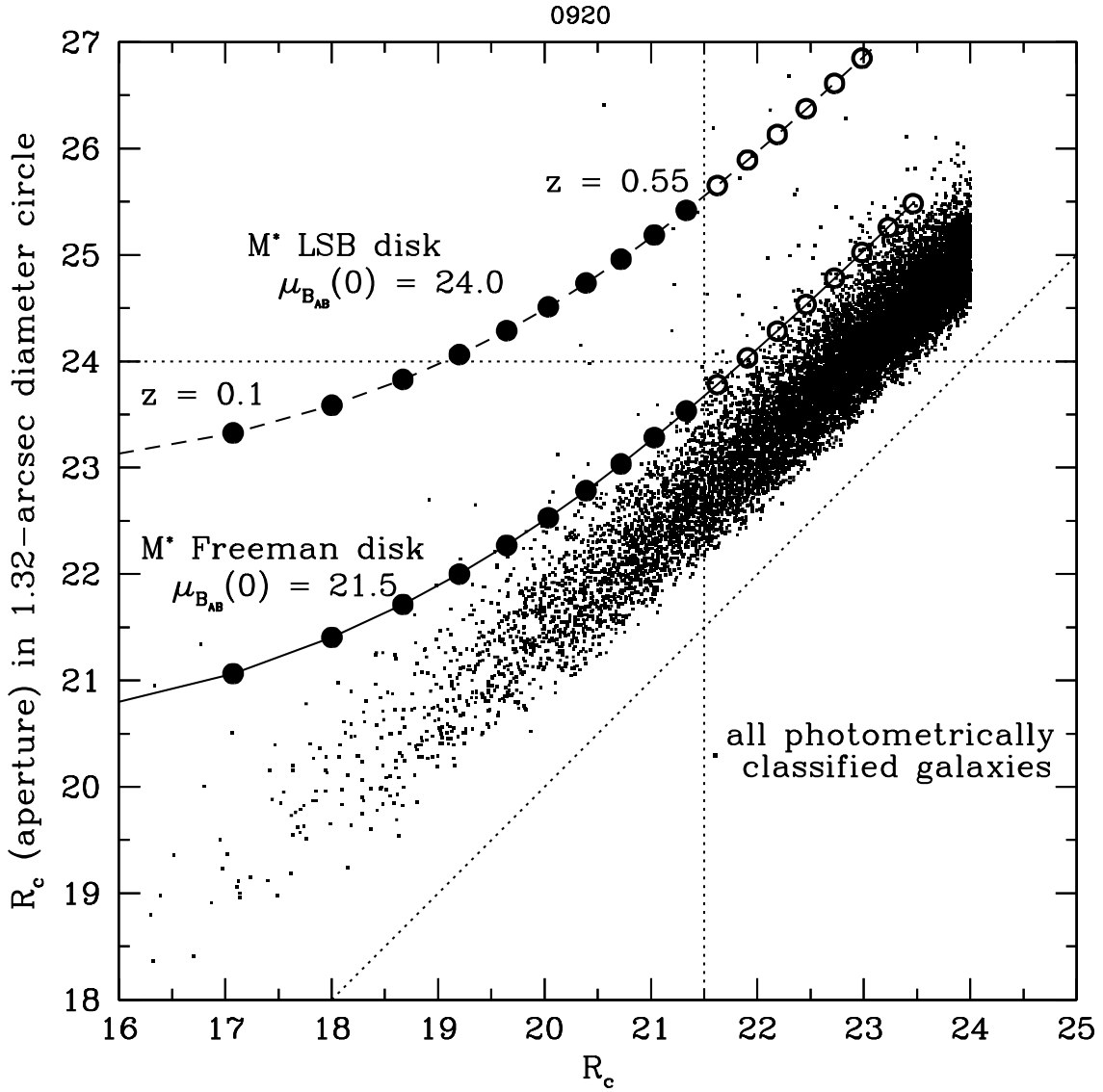


Fig. 2.— Central aperture magnitude $R_c(\text{aperture})$, defined in a $1.32''$ -diameter circle, vs. apparent magnitude R_c , plotted for objects photometrically classified as galaxies or probable galaxies in the CNOC2 0920 patch. The dotted diagonal line is just $R_c = R_c(\text{aperture})$, the dotted vertical line indicates the $R_c = 21.5$ nominal spectroscopic limit, and the dotted horizontal line is the approximate central aperture magnitude limit $R_c(\text{aperture}) = 24.0$ (see discussion in text). Also plotted are the redshift tracks for two face-on disk galaxies, one a Freeman disk (*lower solid curve*) with central surface brightness $\mu_{B_{AB}}(0) = 21.5 \text{ mag arcsec}^{-2}$, and the other a low surface brightness (LSB) disk (*upper dashed curve*) with $\mu_{B_{AB}}(0) = 24.0 \text{ mag arcsec}^{-2}$. Both galaxies have absolute magnitude $M_{B_{AB}} = -19.5 + 5 \log h \approx M^*$. The tracks are calculated for $1''$ seeing and using k -corrections for an Sbc galaxy (CWW). The circles indicate redshifts at intervals $\Delta z = 0.05$, starting at $z = 0.1$ on the left. The filled circles denote the nominal CNOC2 redshift completeness range $0.10 \lesssim z < 0.55$.

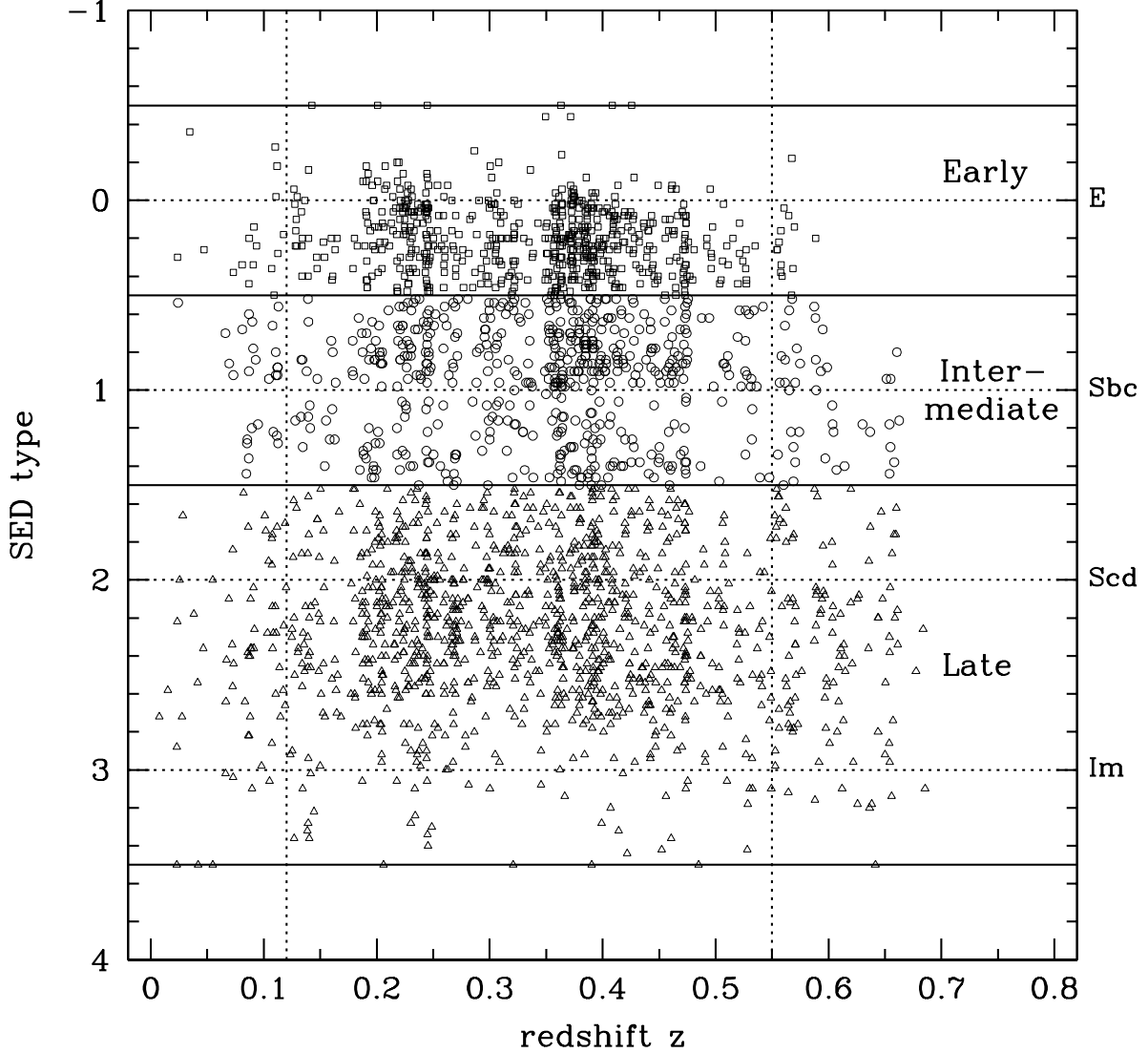


Fig. 3.— Spectral energy distribution (SED) type vs. redshift for CNO2 galaxies with $R_c < 21.5$. The SED types are determined by least-squares fits of $UBVR_cI_c$ magnitudes to those computed from the SED’s of Coleman, Wu, & Weedman (1980; CWW), as described in the text. Numerical SED types for the four original CWW SED’s are assigned as indicated by the dotted horizontal lines, while the boundaries defining the “Early” (*squares*), “Intermediate” (*circles*), and “Late” (*triangles*) CNO2 galaxy categories are indicated by the solid horizontal lines. The dotted vertical lines indicate the CNO2 nominal redshift completeness range $0.12 < z < 0.55$.

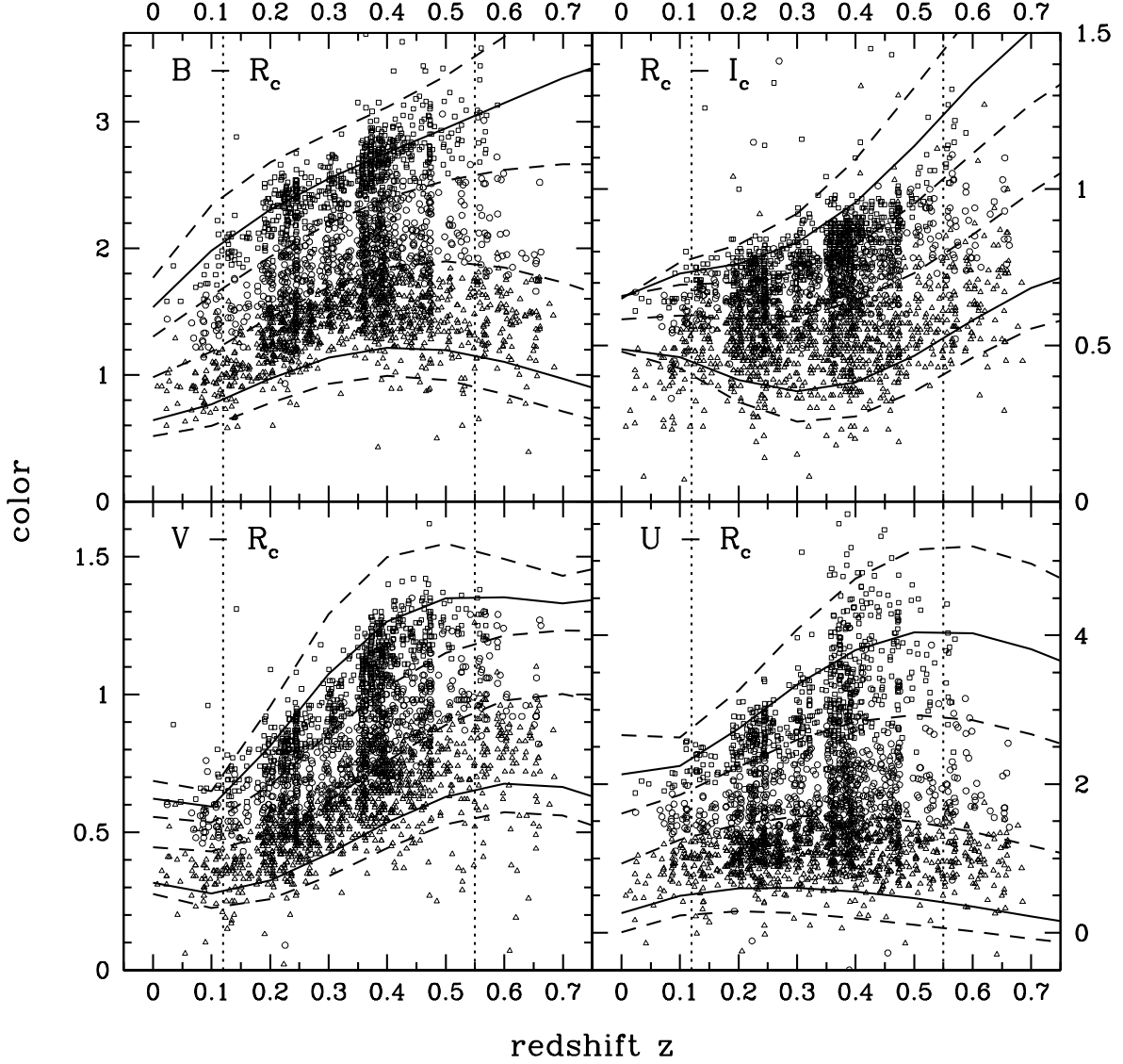


Fig. 4.— Plot of various observed colors vs. redshift for CNOc2 galaxies with $R_c < 21.5$: $B - R_c$ (top left), $R_c - I_c$ (top right), $V - R_c$ (bottom left), and $U - R_c$ (bottom right). The upper and lower solid curves show the colors for the original CWW E and Im SED's, respectively. The dashed curves (corresponding to the solid lines in Figure 3) show the colors for those interpolated and extrapolated CWW SED types which define the boundaries of early (*squares*), intermediate (*circles*) and late (*triangles*) CNOc2 galaxies (the same classifications as in Figure 3). The dotted vertical lines indicate the CNOc2 nominal redshift completeness range $0.12 < z < 0.55$.

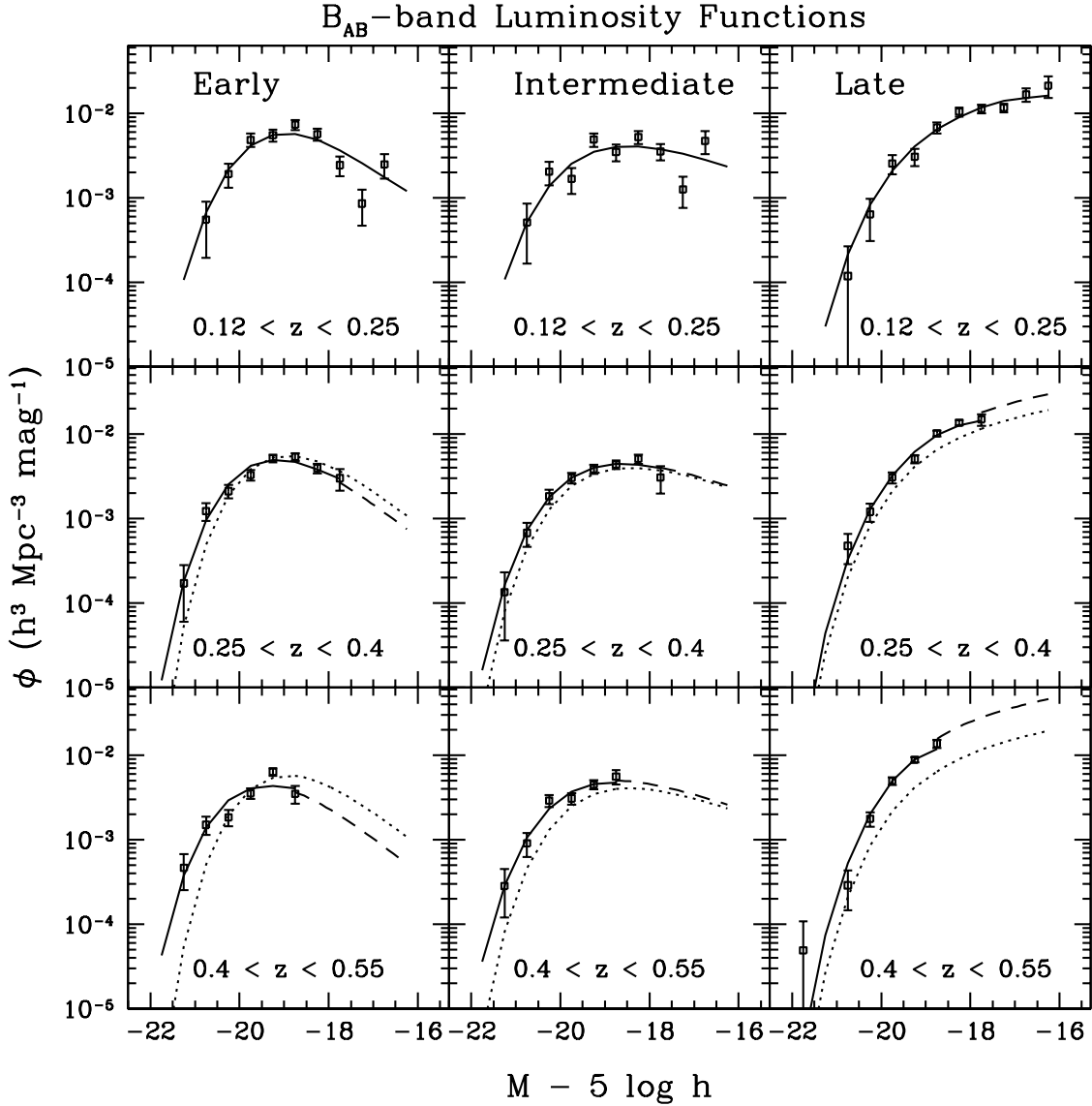


Fig. 5.— B_{AB} -band luminosity functions for early-, intermediate-, and late-type (left to right) CNOC2 galaxies, plotted for the three indicated redshift bins (z increases from top to bottom) in the range $0.12 < z < 0.55$. We show both our best-fit parametric evolving LF models (solid curves) as well as our nonparametric SWML LF estimates (points with 1σ errors). Also shown are fiducial LF's (dotted curves) from the lowest-redshift bin for each galaxy type, and extrapolations (dashed curves) of our best-fit parametric LF to absolute magnitudes fainter than those accessible by the survey in each redshift bin. Results shown are for $q_0 = 0.5$. Please see text for a detailed discussion of the presentation of the data, as there are a number of subtleties involved.

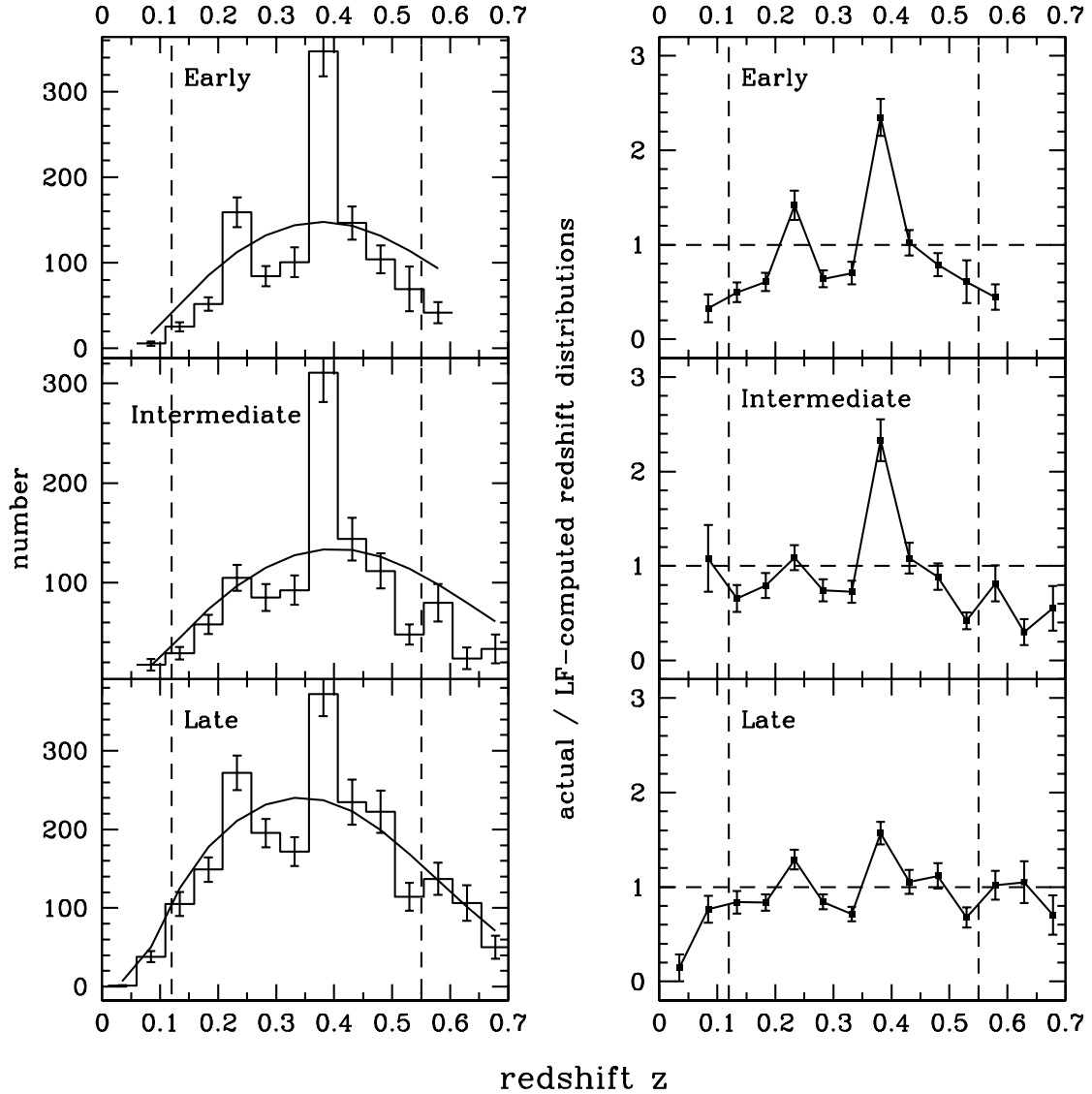


Fig. 6.— (*Left 3 panels*) Weighted redshift histograms for early, intermediate, and late CNOC2 galaxies with apparent magnitudes $17.0 < R_c < 21.5$ and absolute magnitudes $-22 < M_{B_{AB}} - 5 \log h < -16$ ($q_0 = 0.5$). The galaxies have been weighted by the factors W_i defined in equation (2) to correct for incompleteness. The smooth curves are the redshift distributions computed from the best-fit evolving B_{AB} LF model derived in § 4.1. (*Right 3 panels*) The ratio of the actual weighted redshift histogram to the LF-computed redshift histogram. The dashed vertical lines indicate the CNOC2 nominal redshift completeness range $0.12 < z < 0.55$. All uncertainties are computed assuming simple \sqrt{N} errors.

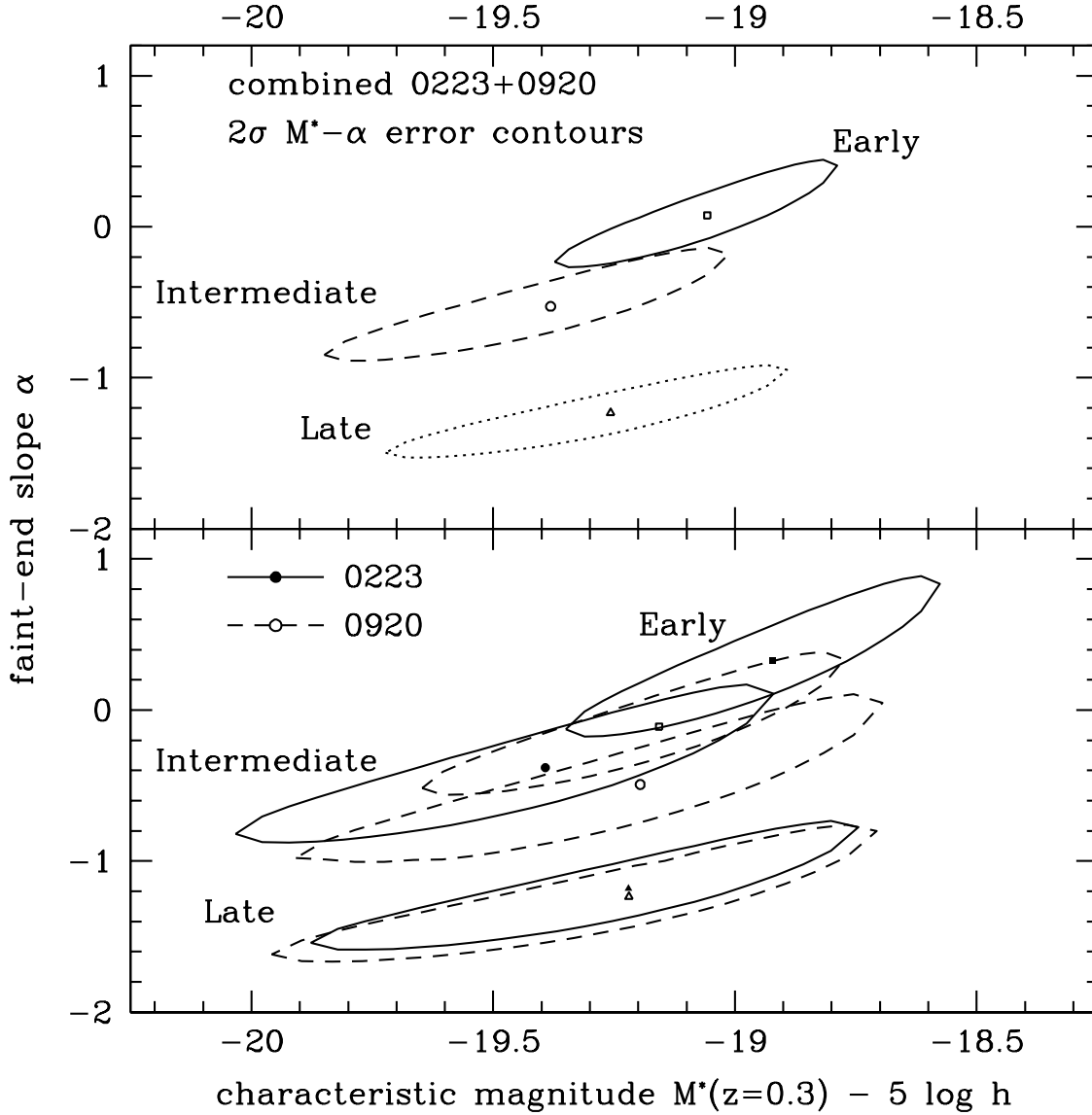


Fig. 7.— 2σ error contours in $M^*(z = 0.3)$ vs. α for the B_{AB} luminosity functions of various CNOC2 samples. (Top) Error contours for early, intermediate, and late types for the full 0223+0920 sample. (Bottom) Comparison of error contours for early, intermediate, and late types for the 0223 (solid contours and filled points) and 0920 (dashed contours and open points) patches.

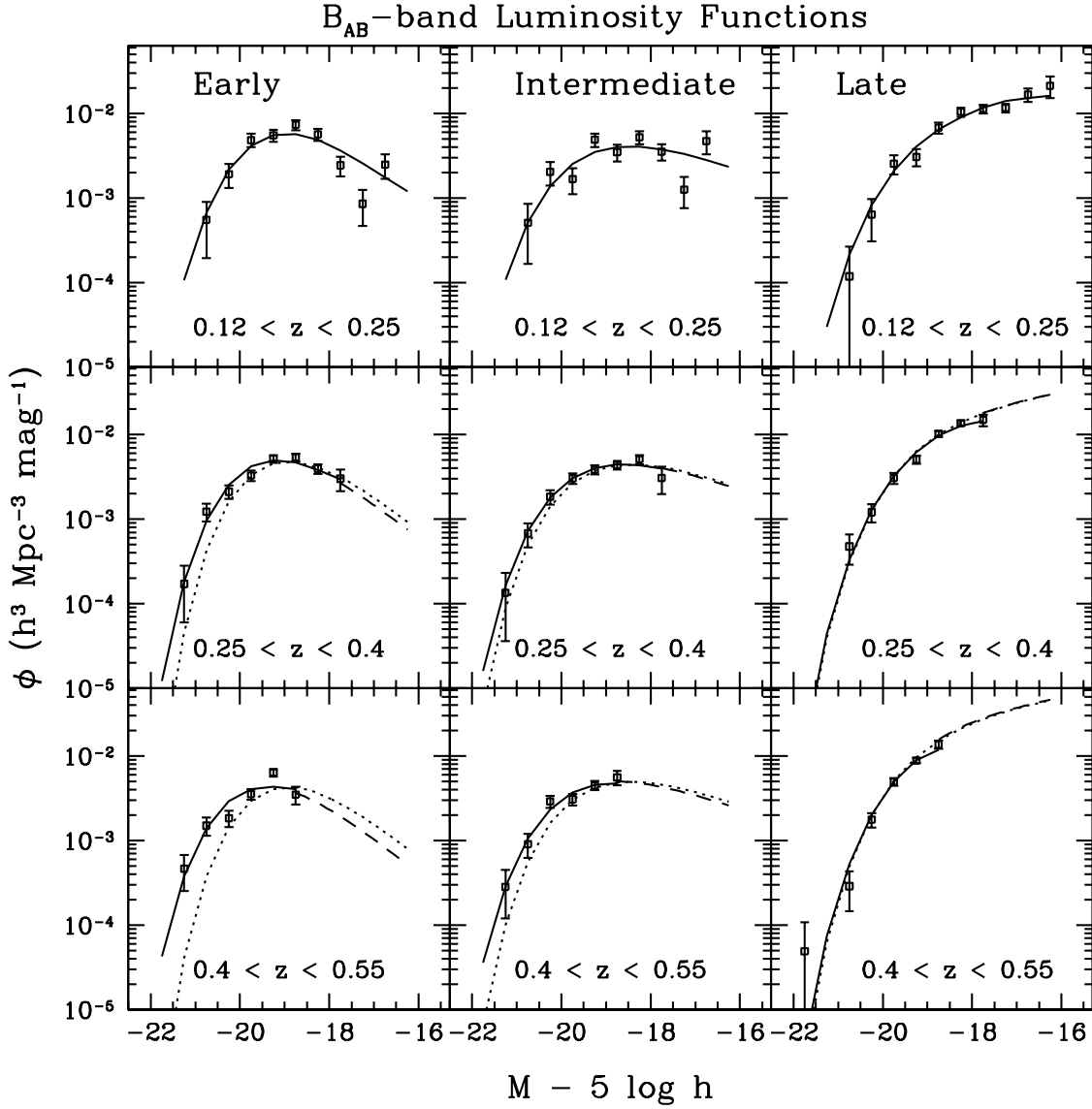


Fig. 8.— Same as Figure 5 but with the fiducial low-redshift LF (*dotted curves*) rescaled to take out the effects of density evolution; see text for details.

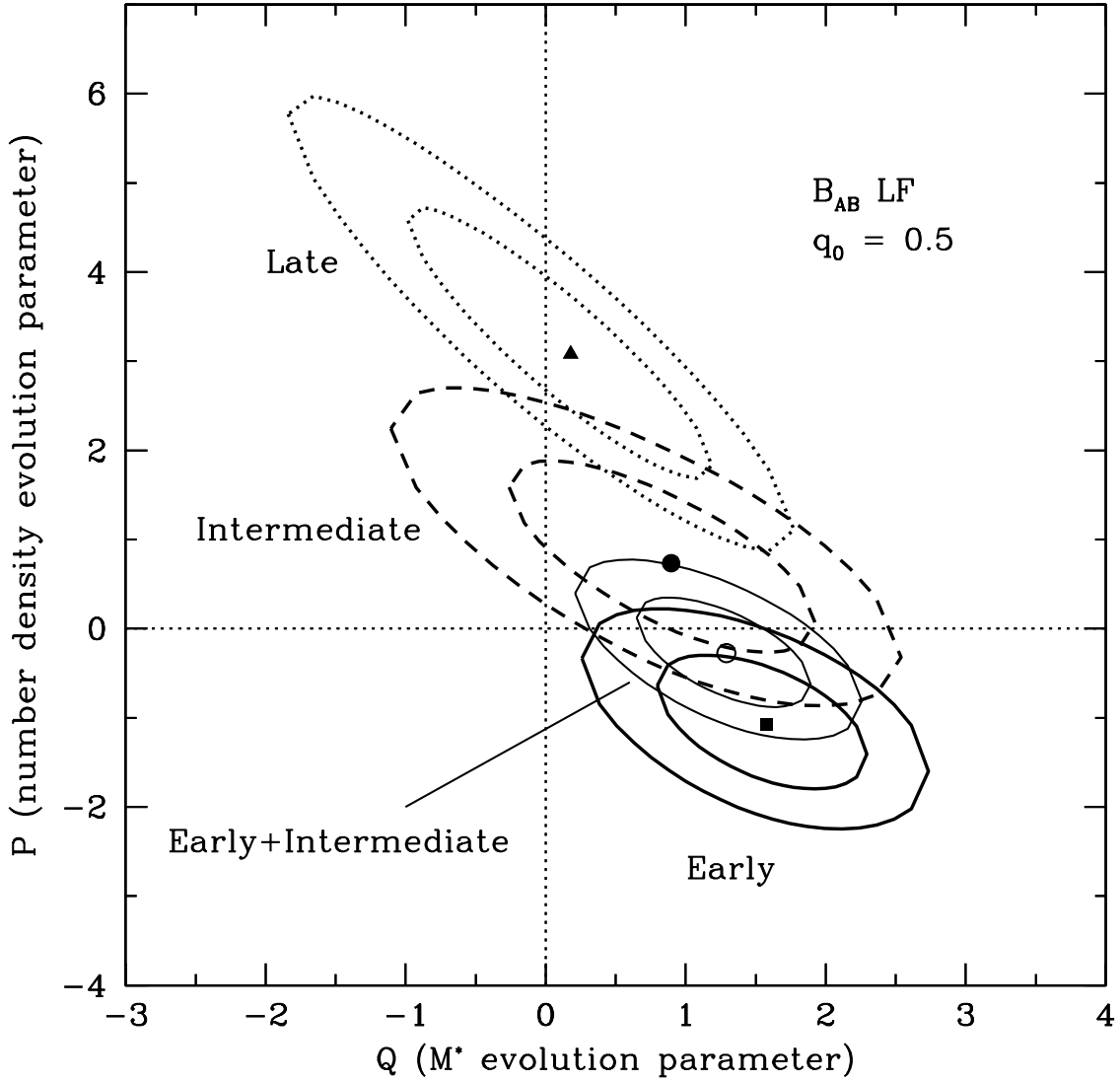


Fig. 9.— 1σ and 2σ error contours in P (number density evolution parameter) vs. Q (M^* evolution parameter) for the B_{AB} luminosity functions of early (*solid contours and filled square*), intermediate (*dashed contours and filled circle*), late (*dotted contours and filled triangle*), and early+intermediate (*light solid contours and open circle*) CNOC2 samples. Results shown are for $q_0 = 0.5$. The intersection of the horizontal and vertical dotted lines indicates no-evolution, $P = Q = 0$.

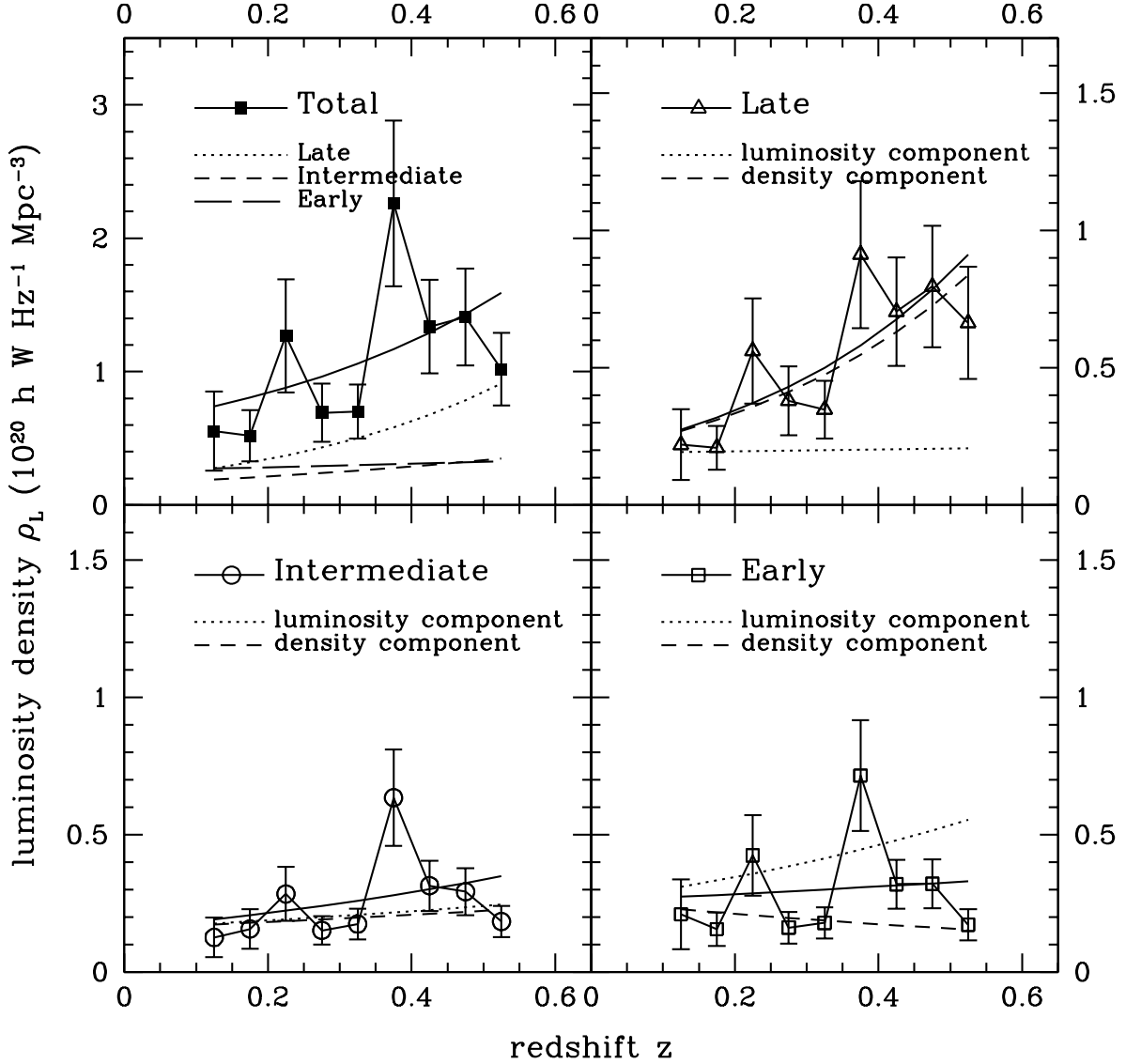


Fig. 10.— Redshift evolution of the CNOC2 rest-frame B_{AB} luminosity density $\rho_L(z)$, shown for the early, intermediate, late, and total galaxy samples. We plot both the directly-observed but LF-weighted (*points*) as well as the LF-computed (*solid lines*) luminosity densities. We also show the separate luminosity-evolution (*dotted curves*) and density-evolution (*dashed curves*) components of the overall LF-computed luminosity density evolution curves. Results shown are for $q_0 = 0.5$.

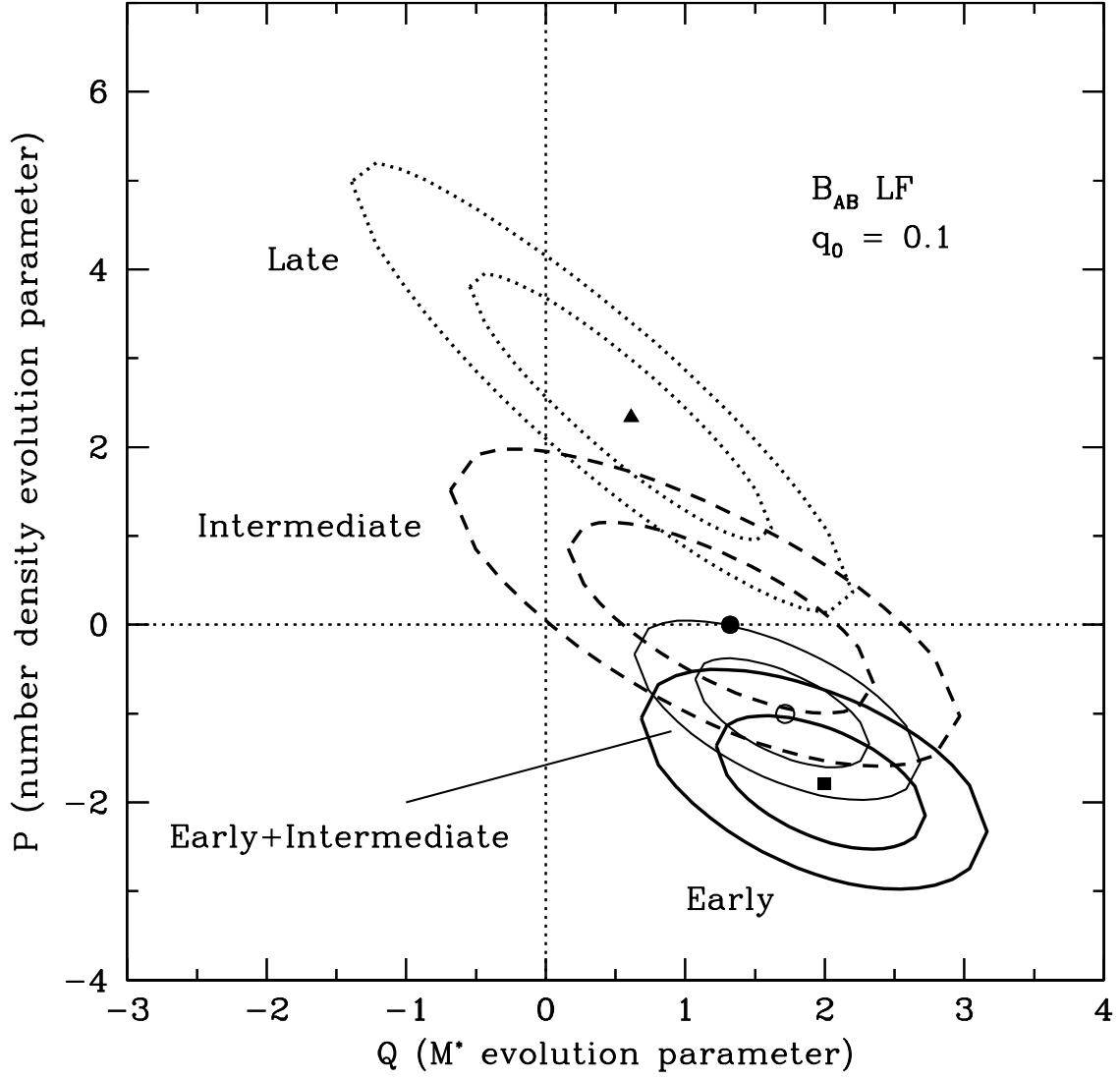


Fig. 11.— Same as Figure 9 but for $q_0 = 0.1$.

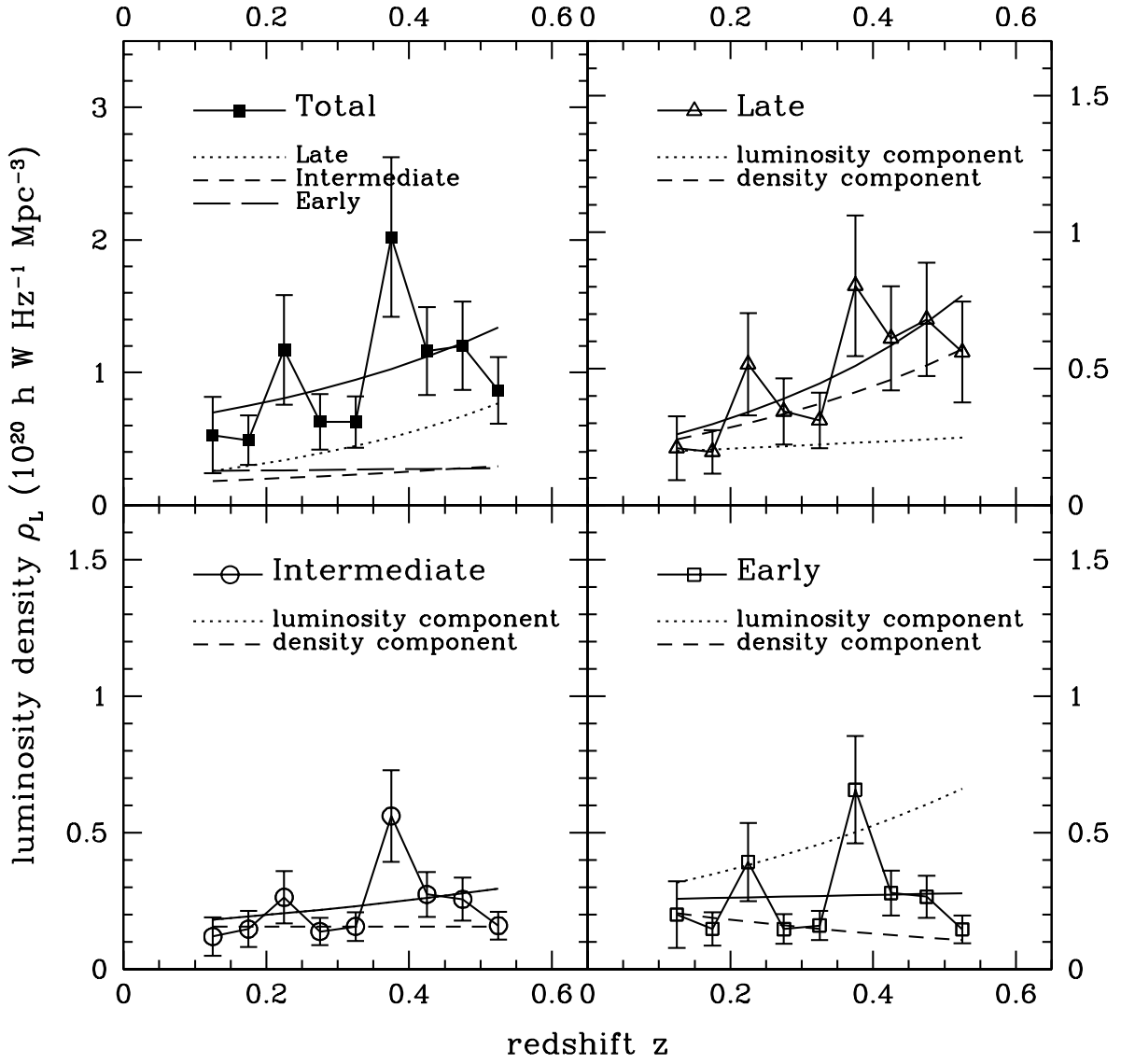


Fig. 12.— Same as Figure 10 but for $q_0 = 0.1$.

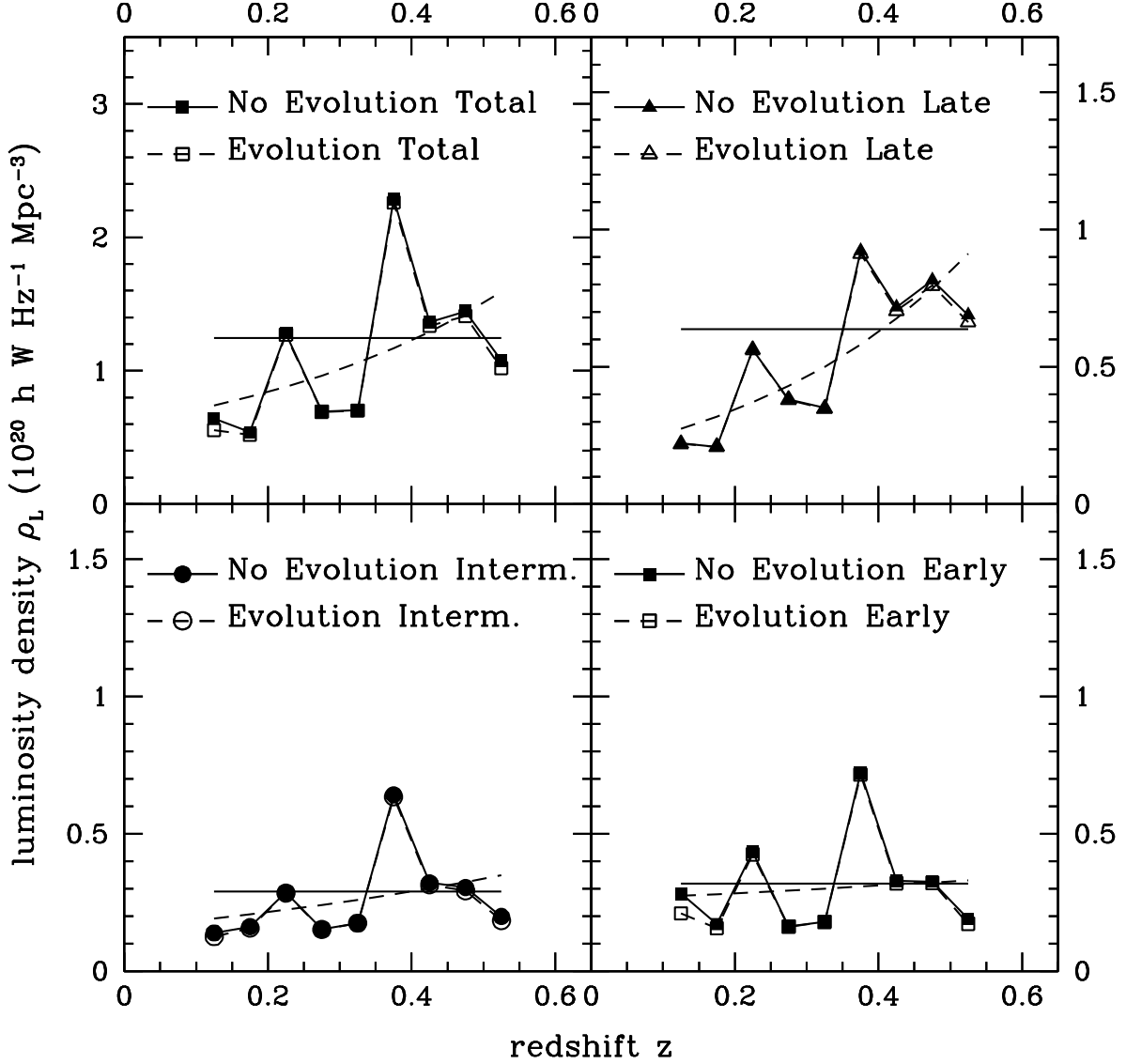


Fig. 13.— Redshift evolution of the CNOC2 B_{AB} luminosity density $\rho_L(z)$, shown for the early, intermediate, late, and total galaxy samples. We plot both the directly-observed but LF-weighted (*points*) and the LF-computed (*lines*) luminosity densities, where the LF’s have been fit using either an evolving model (*dashed curves and open points*), or a non-evolving model (*solid horizontal lines and filled points*) with $P = Q = 0$. Results shown are for $q_0 = 0.5$.

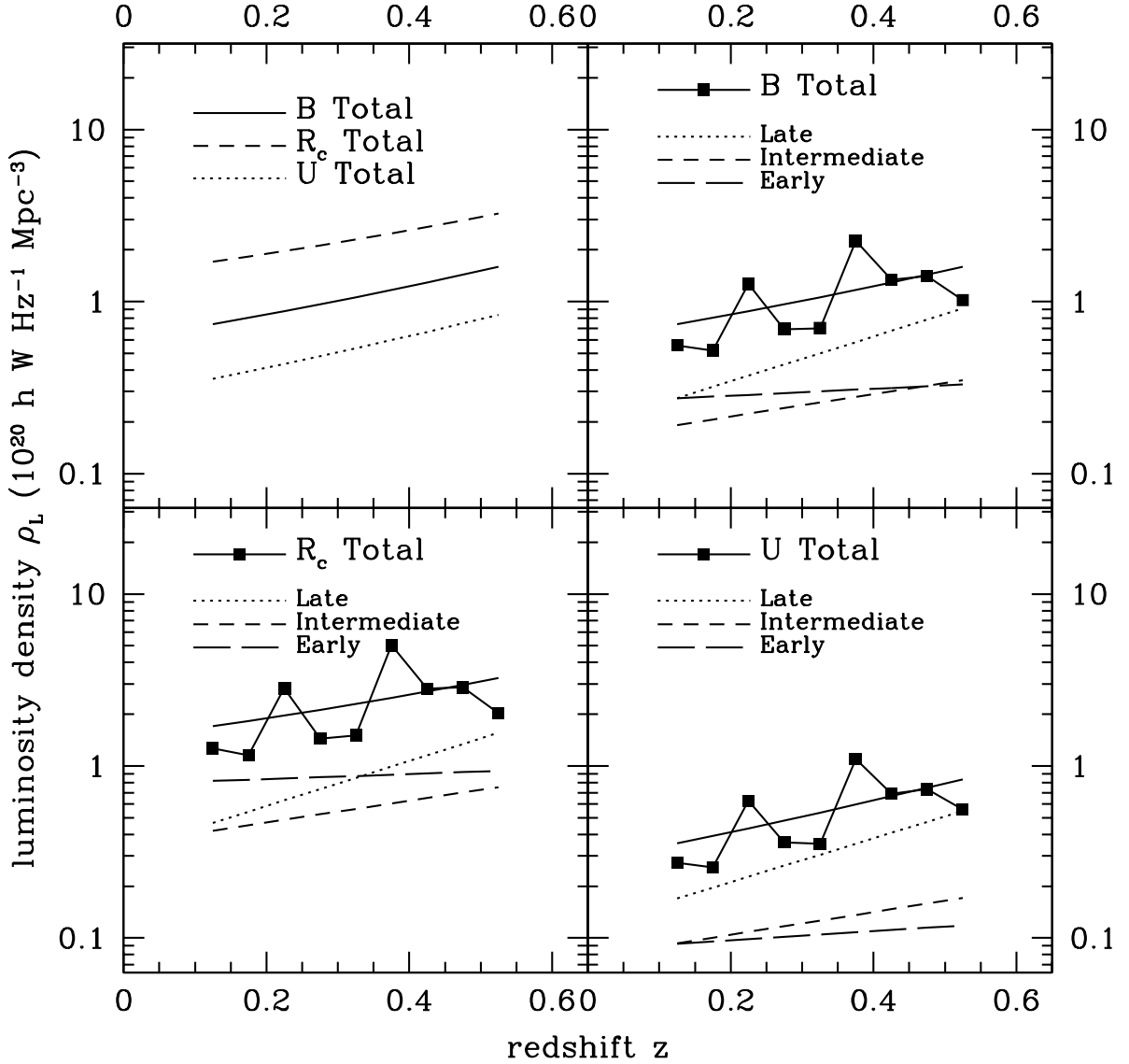


Fig. 14.— Redshift evolution of the CNOC2 rest-frame luminosity density $\rho_L(z)$, shown for the B , R_c , and U bands. The top left panel compares the total $\rho_L(z)$ for the three bands, while the other three panels break down each band into results by galaxy type. Note that unlike in previous figures, ρ_L is plotted here on a logarithmic scale to facilitate comparison of the *rates* of luminosity density evolution among the three different bands.

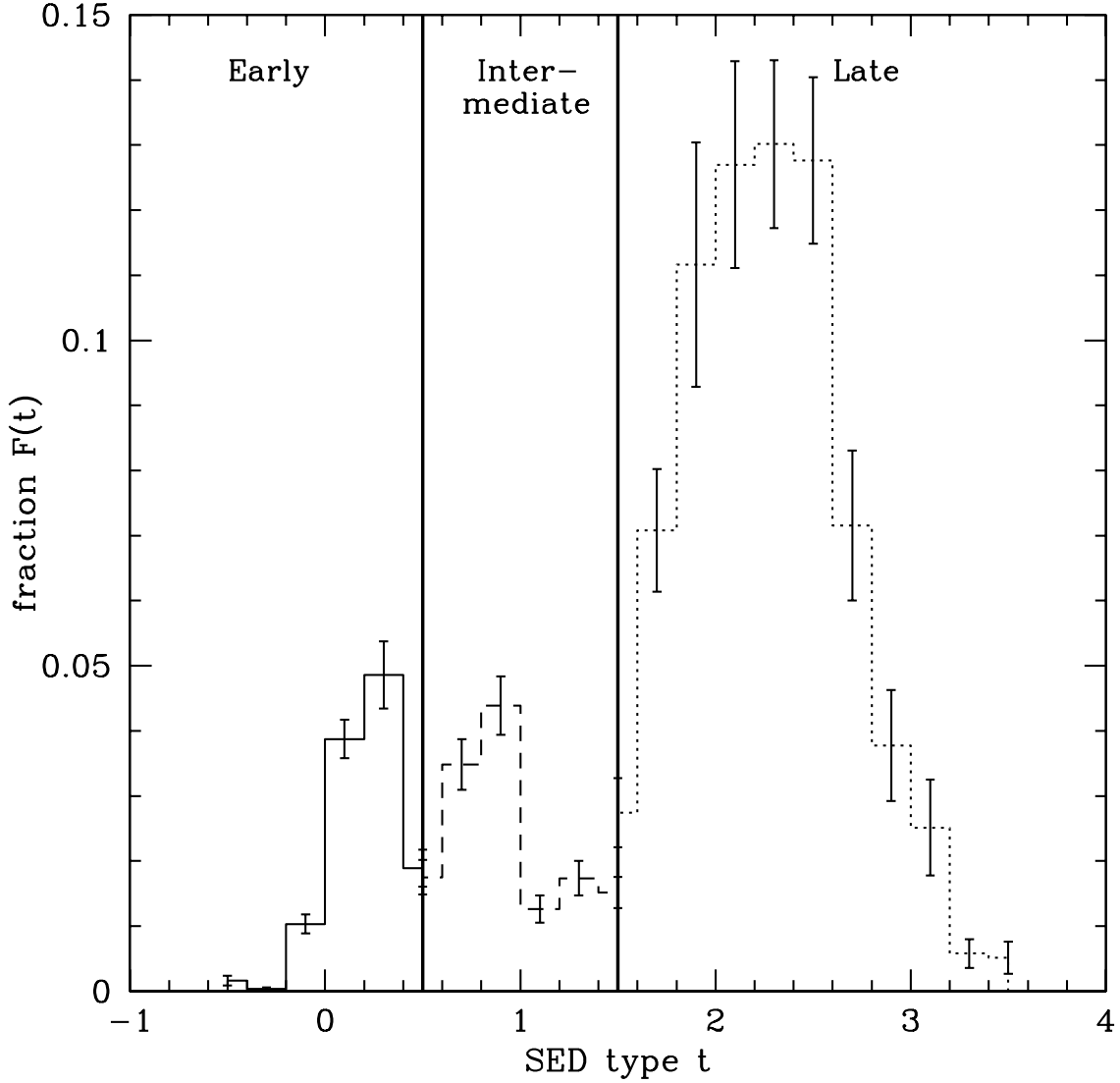


Fig. 15.— Fractional distribution $F(t)$ of SED types t , calculated for the redshift range $0.12 < z < 0.55$ using equation (21) as described in the text. All uncertainties are computed assuming simple \sqrt{N} errors. Note that we have corrected $F(t)$ so that it is appropriate for a *volume-limited* sample with $-22 < M_{B_{AB}} - 5 \log h < -16$; see text for details.

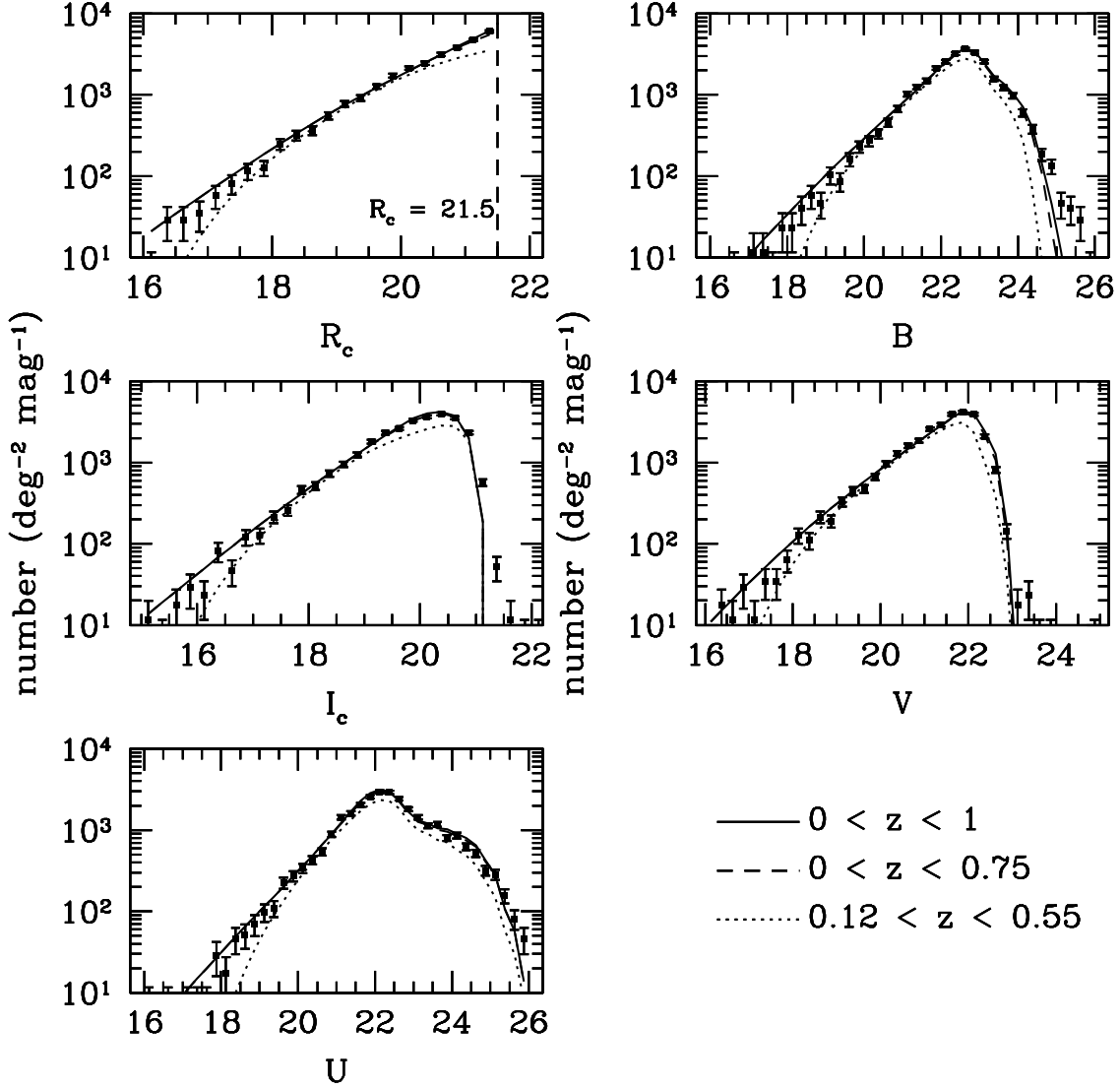


Fig. 16.— The differential galaxy number counts (*points*) for the CNO2 $UBVR_cI_c$ bands, restricted to those galaxies with $R_c < 21.5$. Uncertainties are computed assuming simple \sqrt{N} errors, and thus do not account for fluctuations due to galaxy clustering. Also shown are counts computed from our best-fit evolving B_{AB} LF model, using equation (23) as described in the text. The various curves show the contributions to the counts from galaxies with $0.12 < z < 0.55$ (*dotted curves*), $0 < z < 0.75$ (*dashed curves*), and $0 < z < 1$ (*solid curves*).

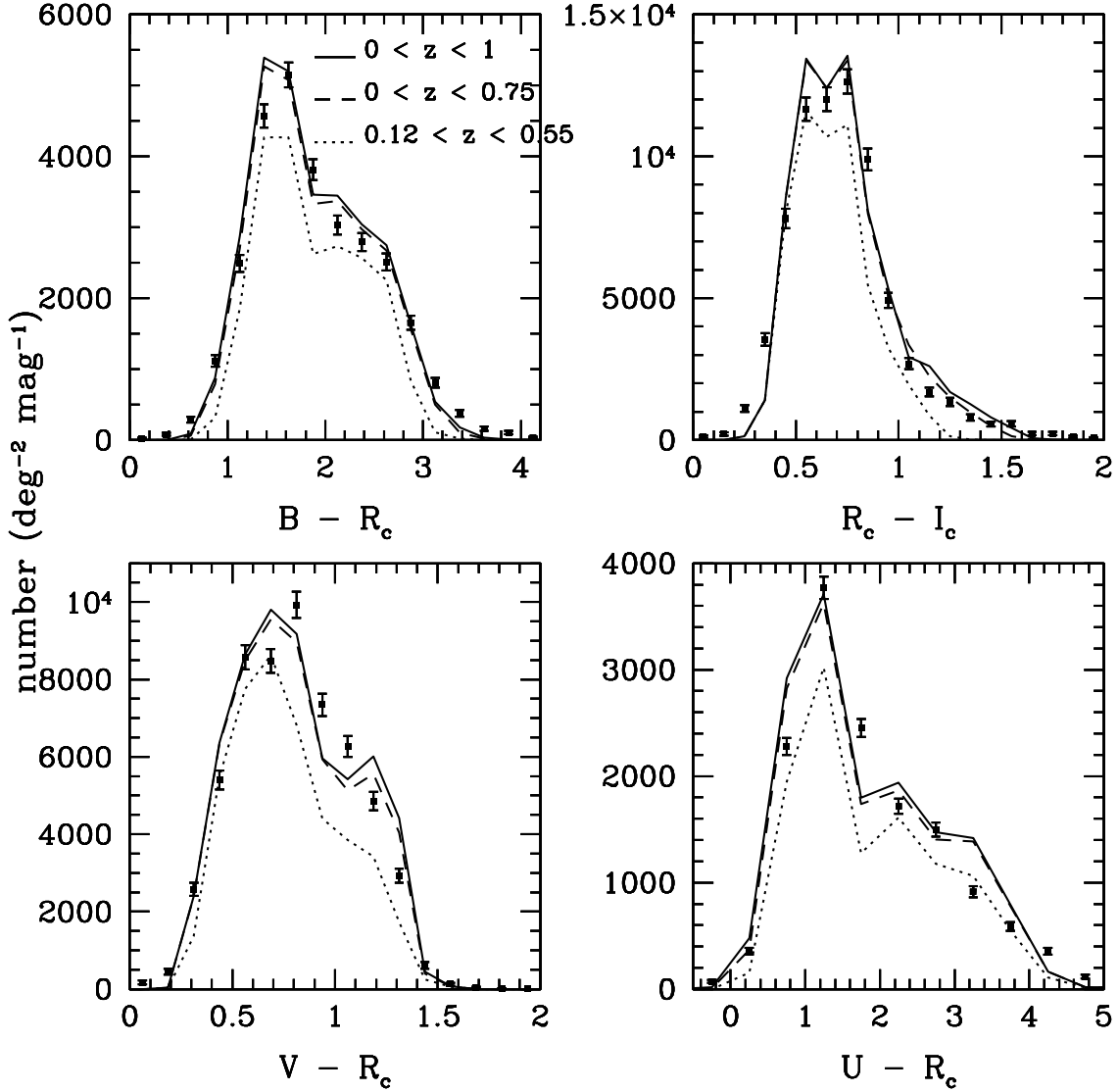


Fig. 17.— The color distributions (*points*) in $B - R_c$, $R_c - I_c$, $V - R_c$, and $U - R_c$, calculated for those CNOC2 galaxies with $R_c < 21.5$. Uncertainties are computed assuming simple \sqrt{N} errors, and thus do not account for fluctuations due to galaxy clustering. Also shown are color distributions computed from our best-fit evolving B_{AB} LF model, for the contributions of galaxies with $0.12 < z < 0.55$ (*dotted curves*), $0 < z < 0.75$ (*dashed curves*), and $0 < z < 1$ (*solid curves*).

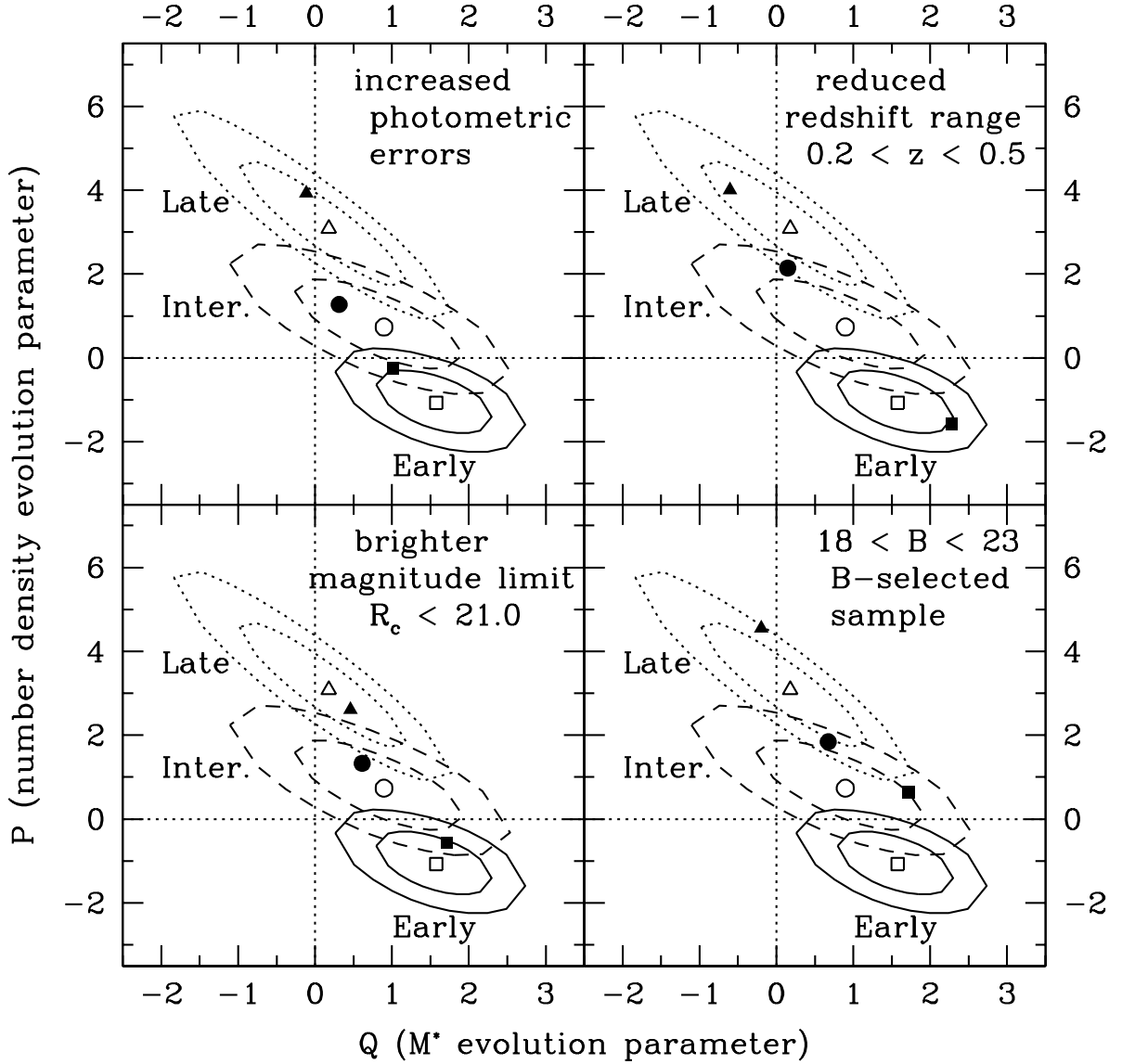


Fig. 18.— The impact of various systematic effects on the best-fit values of P and Q for the B_{AB} LF. The original P - Q values (*open points*) plus 1σ and 2σ contours from Figure 9 are reproduced here. The *solid points* show the modified P - Q values resulting from use of an “error-boosted” sample (*top left*; see text for details), from a reduced redshift range $0.2 < z < 0.5$ (*top right*), from adoption of a brighter magnitude limit $R_c < 21.0$ (*bottom left*), and from use of a B -selected $18 < B < 23$ sample (*bottom right*).

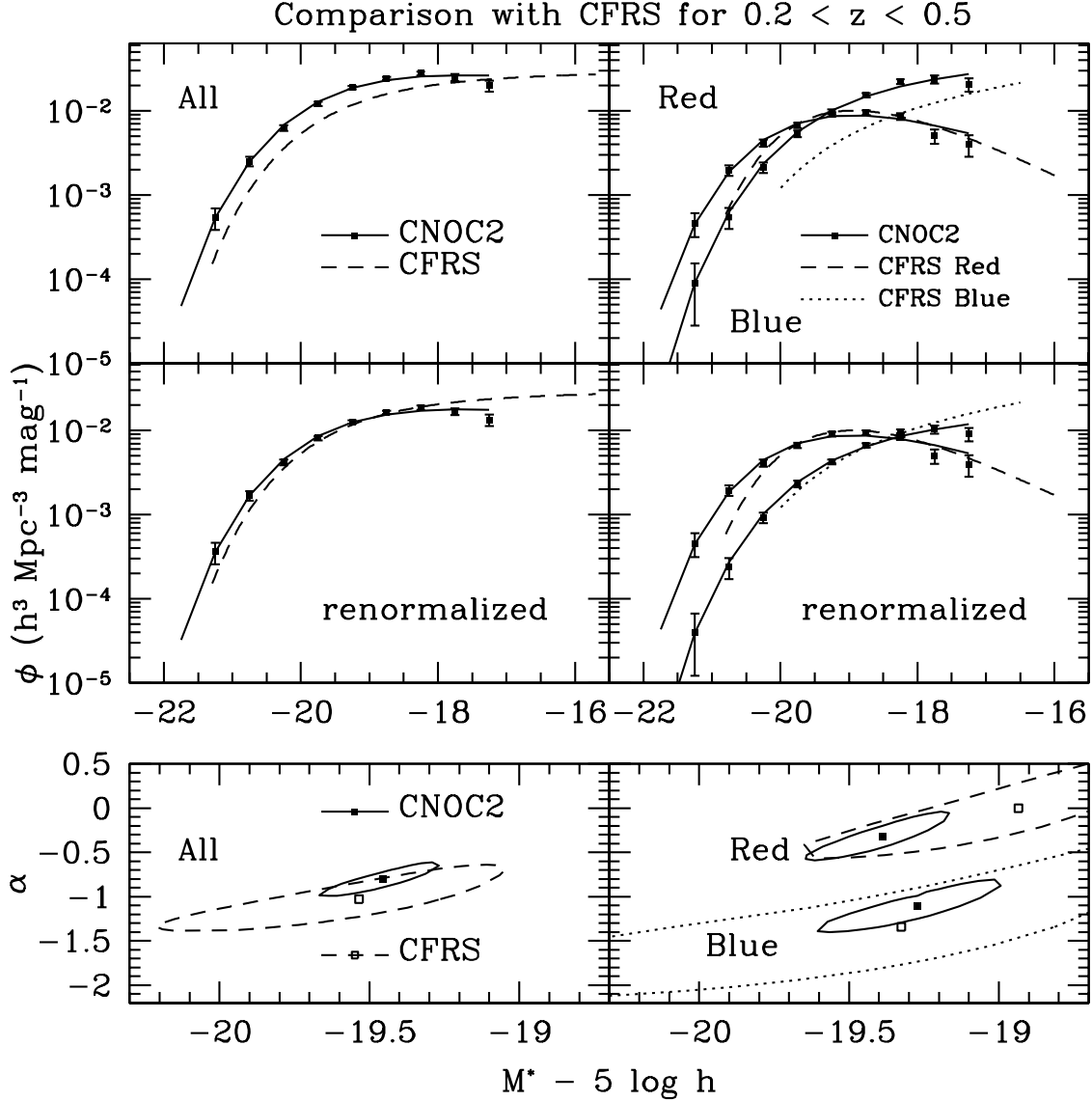


Fig. 19.— (*Top panels*) Comparison of non-evolving B_{AB} LF's for the CNOC2 (*solid curves and filled points*) and CFRS (Lilly et al. 1995a; *dashed and dotted curves*) samples in the overlapping redshift range $0.2 < z < 0.5$. Comparisons are shown for the full galaxy samples (*top left*), and for red and blue galaxy subsamples split at the color/SED of a CWW Sbc galaxy (*top right*). (*Middle panels*) Same as the corresponding top panels except that the CNOC2 LF's have been renormalized to match the CFRS LF's using an analog of equation (20). (*Bottom panels*) 2σ $M^* - \alpha$ error contours for the all, red, and blue CNOC2 and CFRS samples.

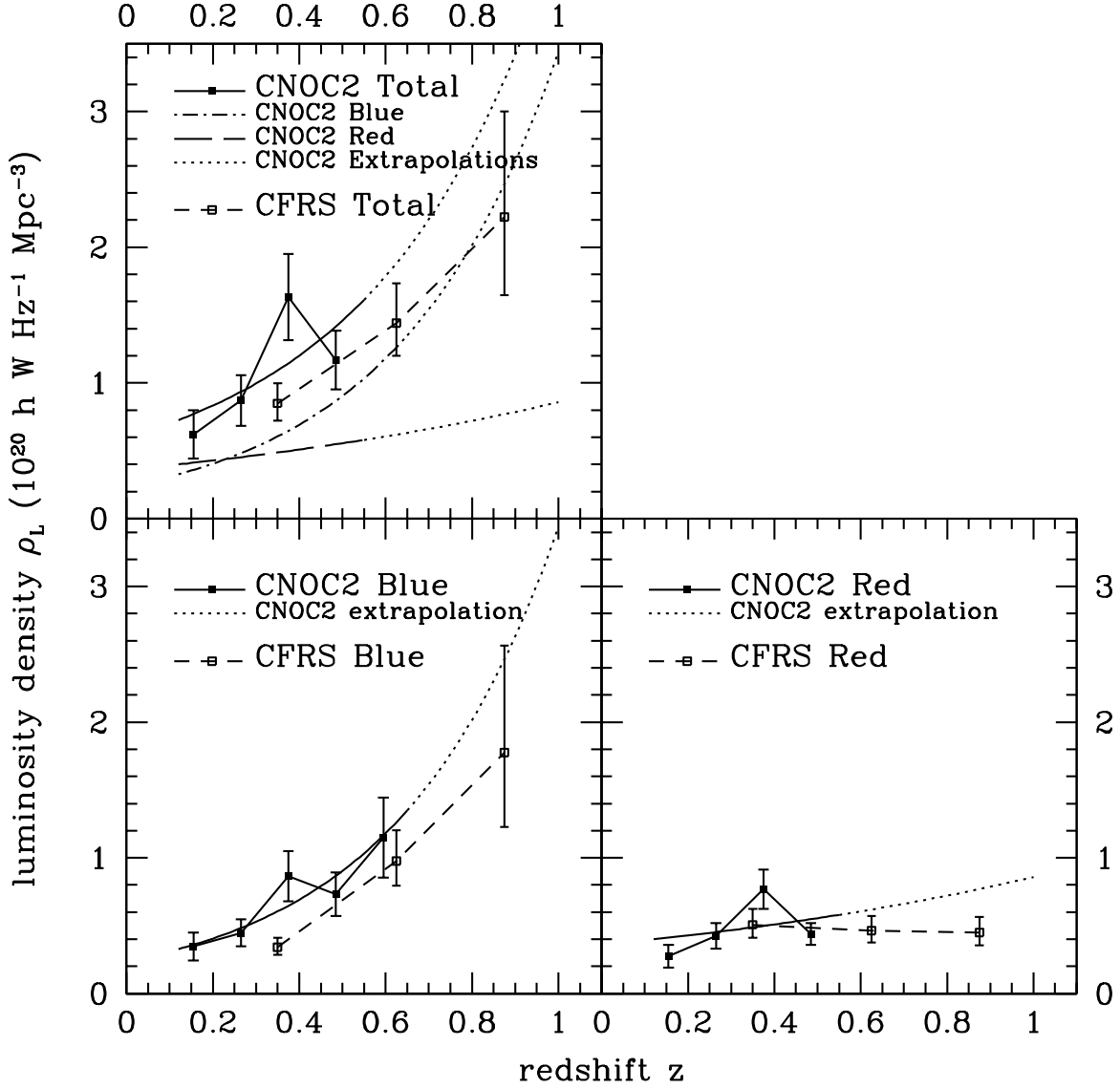


Fig. 20.— Comparison of B_{AB} luminosity densities for the CNOC2 (*solid curves and filled points*) and CFRS (Lilly et al. 1996; *short dashed curves and open points*) samples. The CNOC2 results are obtained using our usual 5-parameter LF evolution model, but now fit for blue (*bottom left*) and red (*bottom right*) CNOC2 galaxy samples split at the color/SED of a CWW Sbc galaxy. Note that the blue CNOC2 sample is defined for an extended redshift completeness range $0.12 < z < 0.65$; the red galaxy sample covers the usual $0.12 < z < 0.55$ CNOC2 redshift range. The *dotted curves* in the bottom panels show extrapolations of the CNOC2 LF fits beyond the redshift ranges indicated above. The *top left panel* compares the sum of the red and blue luminosity densities for the CNOC2 and CFRS data sets, and the individual CNOC2 blue and red galaxy $\rho_L(z)$ fits and extrapolations are also shown as indicated in the panel legend.

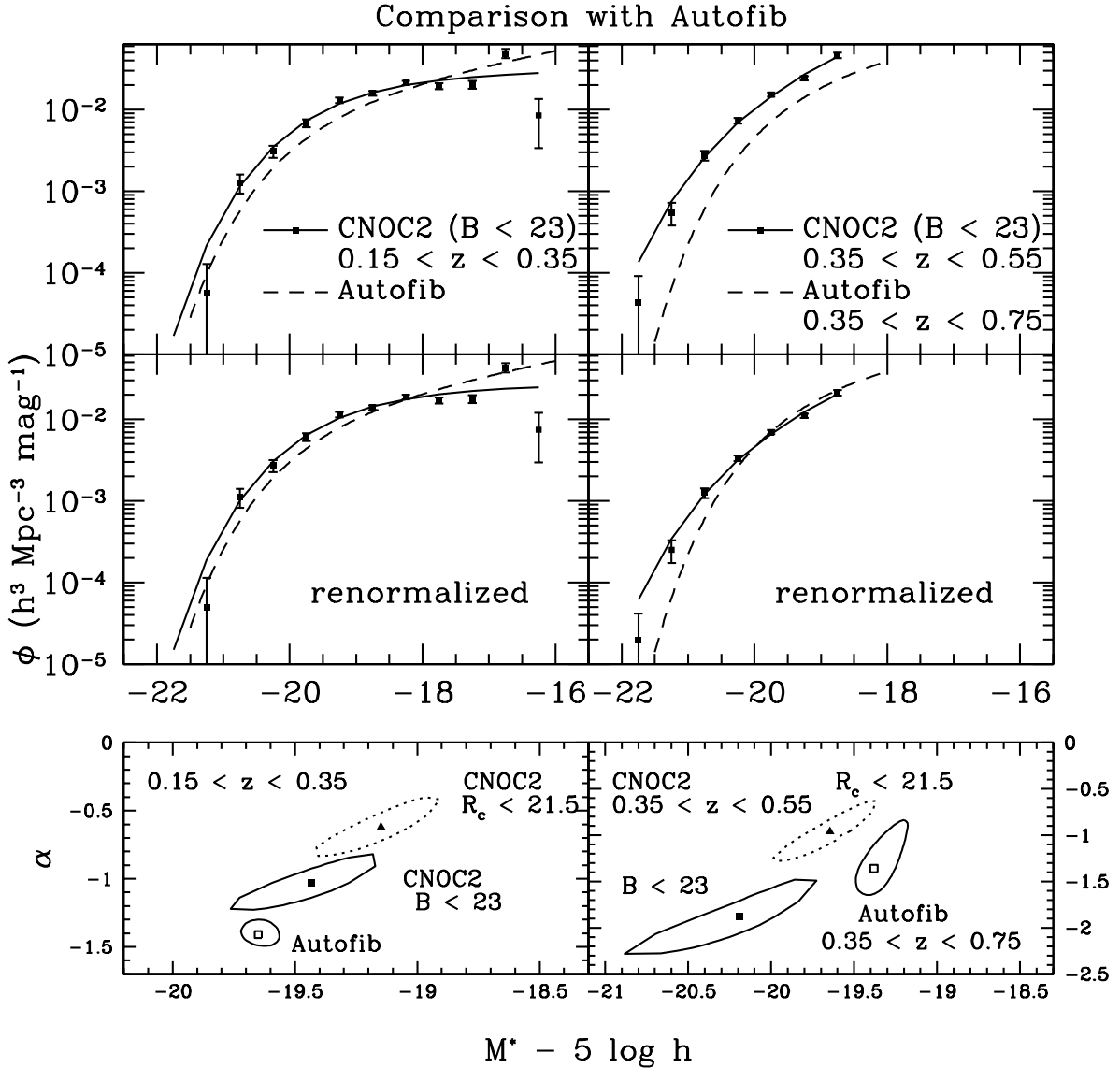


Fig. 21.— (Top panels) Comparison of non-evolving B LF's for the CNOC2 (solid and curves and filled points) and composite Autofib (Ellis et al. 1996; dashed curves) samples in the redshift ranges $0.15 < z < 0.35$ (left panels) and $0.35 < z < 0.75$ (right panels). Unlike previous plots, the CNOC2 LF's have been computed using a $18 < B < 23$ sample to better match the B -selected Autofib sample (see text). (Middle panels) Same as the corresponding top panels except that the CNOC2 LF's have been renormalized to match the Autofib LF's using an analog of equation (20). (Bottom panels) 2σ M^* - α error contours for the CNOC2 and Autofib (solid contours and open squares) LF's. Note that CNOC2 results for both our $18 < B < 23$ (solid contours and filled squares) and our standard $17 < R_c < 21.5$ (dotted contours and filled triangles) samples are shown.